Selective reductive conversion of CO_2 to CH_2-bridged compounds by using a Fe-functionalized graphene oxide-based catalyst

Check for updates

Swarbhanu Ghosh [1] & Parisa A. Ariya [1,2] ✉

Anthropogenic climate change drastically affects our planet, with CO_2 being the most critical gaseous driver. Despite the existing carbon dioxide capture and transformation, there is much need for innovative carbon dioxide hydrogenation catalysts with excellent selectivity. Here, we present a fast, effective, and sustainable route for coupling diverse alcohols, amines and amides with CO_2 via heterogenization of a natural metal-based homogeneous catalyst through decorating on functionalized graphene oxide (GO). Combined synthetic, experimental, and theoretical studies unravel mechanistic routes to convergent 4-electron reduction of CO_2 under mild conditions. We successfully replace the toxic and expensive ruthenium species with inexpensive, ubiquitously available and recyclable iron. This iron-based functionalized graphene oxide (denoted as Fe@GO-EDA, where EDA represents ethylenediamine) functions as an efficient catalyst for the selective conversion of CO_2 into a formaldehyde oxidation level, thus opening the door for interesting molecular structures using CO_2 as a C1 source. Overall, this work describes an intriguing heterogeneous platform for the selective synthesis of valuable methylene-bridged compounds via 4-electron reduction of CO_2.

Since Diesel discovered the first application in a combustion-ignition engine in 1895[1], industries have employed diesel fuel in motor vehicles, construction machines, and transportation[2,3]. Liquid diesel fuels now account for 95% of transport energy in compression ignition (CI) engines and power 99.8% of worldwide transportation, three because it outperforms gasoline in terms of torque output and fuel efficiency for spark ignition (SI) engines, particularly in mid- and heavy-duty applications. Yet, CI engines have a severe problem with particulate matter emissions, like soot[4], in addition to greenhouse gas emissions and other cytotoxicity issues associated with diesel exhaust[5–7].

Several alternatives like battery electric vehicles, biofuels, and hydrogen have arisen in recent years[8,9]. While battery electric vehicles are an attractive option for short-distance transportation[10], high-energy density fuels are likely to be required for long-distance transportation for the foreseeable future. Recent studies demonstrate that adding oxygen-containing chemicals to diesel fuel, such as oxymethylene ether (OME), ethanol, and dimethyl carbonate, efficiently reduces soot emissions[11–13]. This precludes not only diesel engine modification but also pollution reduction in the diesel exhaust through the appropriate inclusion of fuel additives; simple alcohols or ethers, on the other hand, do not meet these standards. Oxymethylene ethers are -O-CH_2-linked oligomers that have gained considerable attention in recent decades because of their inherent properties that could be exploited as fuel additives[14–16]. Among the OMEs, methylal or dimethyoxymethane (DMM) is the first member in the homologous series[17–28]. We can utilize DMM not only in the perfume and pharmaceutical industries and as a green solvent but also as a fuel additive or a precursor to producing OMEs by reacting with formaldehyde[29,30]. Industrially, DMM is made in a two-step process where heterogeneous mixed-metal catalysts and the latter step catalyze the former from methanol to formaldehyde. Thereby, a conversion of formaldehyde to DMM is mediated by the acid catalysts (Formox process)[31] or fluid-bed reactor-based process for the synthesis of OMEs from DMM and formaldehyde[32,33].

[1]Department of Chemistry, McGill University, Montréal, QC, Canada. [2]Department of Atmospheric and Oceanic Sciences, McGill University, Montreal, QC, Canada. ✉e-mail: parisa.ariya@mcgill.ca

A [Ru]-based molecular catalyst in a solution state can facilitate DMM synthesis in one pot via oxidation followed by condensation[34]. The reductive method of producing the central CH_2 unit from CO_2 using eco-friendly catalyst will be more attractive because the sustainable conversion of CO_2 into fuels and other value-added chemicals is not only economically beneficial but also crucial from an environmental viewpoint[35–40]. Numerous reports described CO_2 reductive functionalization using hydrosilanes to the corresponding formaldehyde level product such as bis(silyl)acetals[41–43]. Klankermayer et al. developed a metal-based protocol for DAM synthesis from CO_2, alcohols and molecular hydrogen using Ru-based molecular catalyst through his fundamental and pioneering work (Fig. 1, A)[19]. Inspired by these results, Klankermayer's group established an elegant strategy for DMM production from CO_2, molecular hydrogen and methanol using a cobalt-containing system (Fig. 1, B)[21]. After those significant reports, Trapp et al. introduced a new methodology for this conversion[20]. These outstanding outcomes inspire the authors to explore further their investigations to related backbone-modified tripodal ligand systems having a phosphorous (H, where R = P) or silicon (F and G, where R = Si-Ph and Si-Me, respectively)[44]. Among the various systems, Ru(^{Me}Si-Triphos^{Ph}) coupled with Al(OTf)$_3$ (Fig. 1, G) offers the best outcomes for the synthesis of DMM, although without surpassing more active system (Fig. 1, E)[45]. Very well-connected with this study, the same research group displays the power that multivariate modeling optimization can offer for further improvement of the efficiency of a catalytic method[45]. Subsequently, Hashmi et al. developed a related RuH$_2$(Triphos)(PPh$_3$) system, in combination with Al(OTf)$_3$ as acid cocatalyst, for the synthesis of DMM from CO_2, MeOH and molecular hydrogen (Fig. 1, I)[25]. On the other hand, Cantat's group introduced the first

metal-free approach for the four-electron reductive functionalization of CO_2 using amines (Fig. 1, J)[46]. More recently, Mandal et al. demonstrated stable mesoionic N-heterocyclic imines (mNHIs) bearing a highly polarized exocyclic imine for the metal-free reductive functionalization of CO_2 into aminals under the reductive pathway (Fig. 1, K)[47]. Although the approaches mentioned above are attractive and take science to a more advanced level, the usage of homogeneous medium has limited potential for large-scale synthesis. Recently, other researchers introduced heterogeneous reductive functionalization of CO_2 to oxymethylene dimethyl ethers using Ru-based catalysts (Fig. 1, L and M)[23,48]. Unfortunately, these heterogeneous approaches require higher temperatures for activation and selective conversion of CO_2. The toxic and expensive ruthenium-based catalysts potentially hamper their commercialization process. Hence, a promising protocol needs to be developed for the reductive functionalization of CO_2 to fuel based on heterogeneous, recyclable, inexpensive and eco-friendly catalyst; thereby, knowledge acquired in metal-promoted catalysis can be utilized for potential sustainable applications.

Building on the fundamental studies, we hypothesize that ethylenediamine-functionalized graphene oxide (GO-EDA) could be constructed through direct immobilization on GO for its applications in heterogeneous metal-based catalytic transformations. Ru or Fe species can be deliberately decorated on a layered functionalized GO via the post-synthetic modification of the GO-EDA using FeO/α-Fe$_2$O$_3$ nanorods and RuCl$_3$ to utilize the recyclable active metal sites for the reductive functionalization of CO_2 into dialkoxymethane (DAM) and aminals. In concurrence with our hypothesis, here, we present the synthesis, theoretical modeling, and comprehensive characterization of Fe@GO-EDA and Ru@GO-EDA
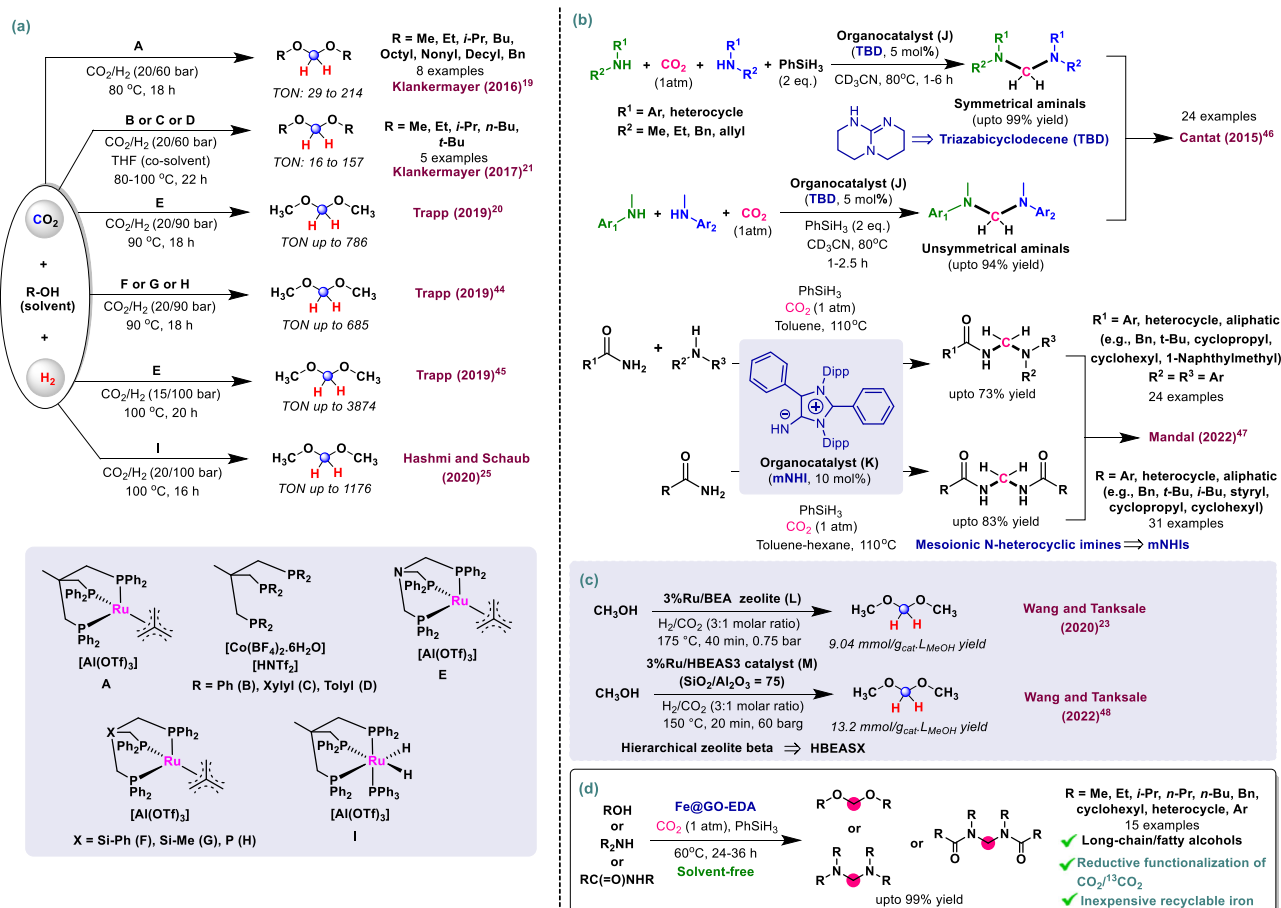

Fig. 1 | Background and motivation of reductive functionalization of CO_2.
a, b Previous reports on the catalytic reductive functionalization of CO_2 to CH_2-bridged compounds using homogeneous catalytic systems. **c** Previous reports on the catalytic reductive functionalization of CO_2 to CH_2-bridged compounds using

heterogeneous catalytic systems. **d** Our work on heterogeneous metal-based reductive functionalization of CO_2 to OMEs, aminals and other CH_2-bridged compounds under atmospheric conditions.
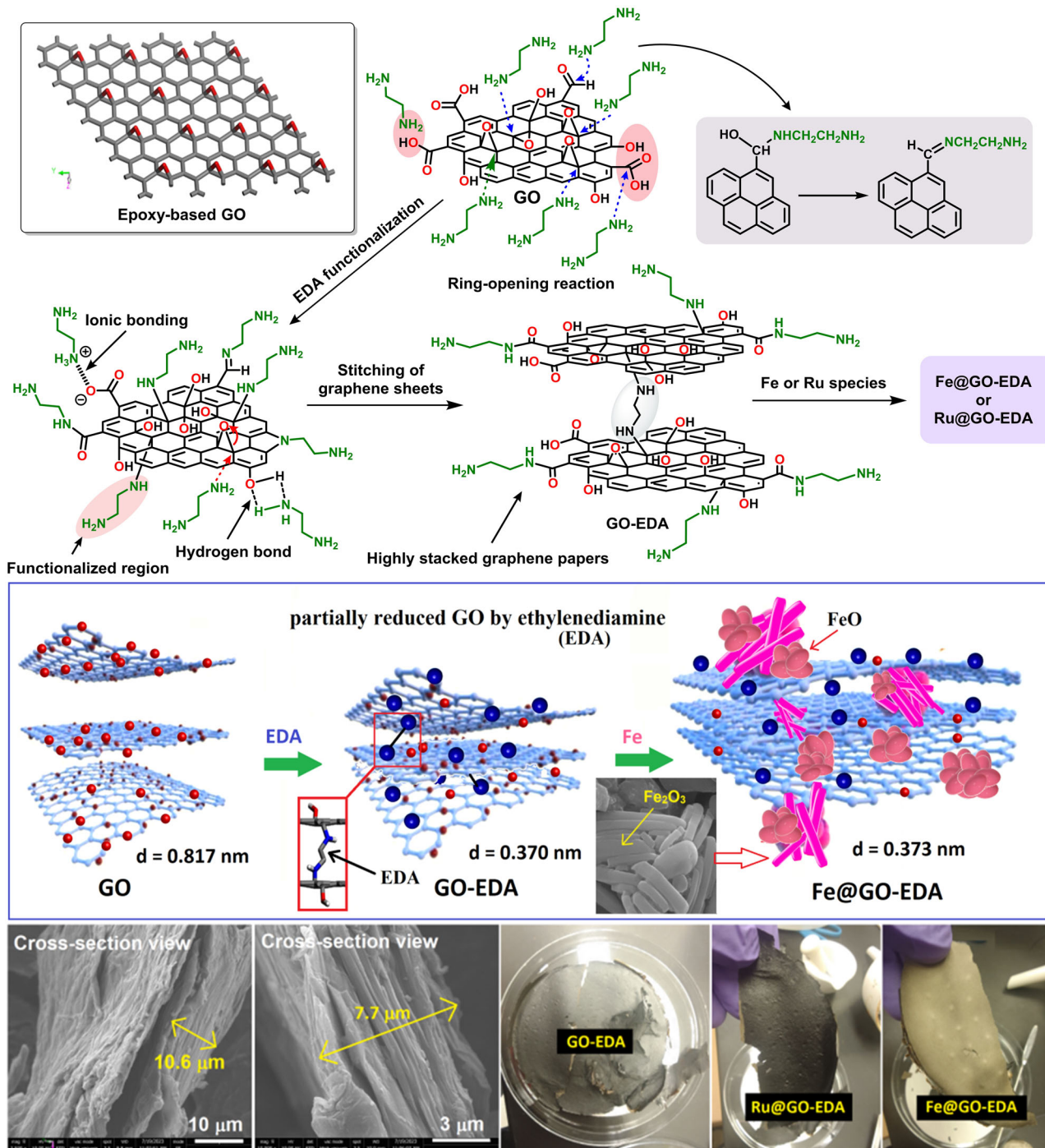
Fig. 2 | The schematic illustration for the synthesis of the EDA-functionalized GO and the Fe- and Ru-based functionalized GO.

synthesized from direct immobilization of EDA on GO sheets under solvothermal conditions, followed by metal decoration.

These metal-functionalized graphene oxide-based materials act as efficient catalysts, allowing for the selective four-electron reduction of CO_2 into a formaldehyde oxidation level. The essence of being thermodynamically favorable with 6-electron reduction and kinetically favorable with four-electron reduction (another challenge) elucidates the exceptional selectivity of CH_2-bridged compounds. More intriguingly, iron is highly sustainable and environmentally friendly. Iron is one of the most recycled metals and typically produces the same quality product after recycling. Considering sustainability, we expand this methodology with an optimal eco-friendly iron-based catalyst (i.e. Fe@GO-EDA).

Results and discussion

Synthesis and characterization of graphene oxide-based materials

The synthesis of the EDA-functionalized GO and the Fe- and Ru-based functionalized GO is depicted in Fig. 2. First, the PXRD measurements are used to evaluate the exact structure of functionalized GO materials, revealing the formation of layered structures. The X-ray diffraction (XRD) data of the GO-EDA, Fe@GO-EDA and Ru@GO-EDA samples and the corresponding d-spacing are depicted in Fig. 3a. The synthesized GO exhibits a prominent peak located at around $2\theta = 10.8°$ (Supplementary Fig. 2) and the measured interlayer distance is about 0.817 nm, which can be due to the formation of various oxygenic functional groups on the basal plane of the graphite[49,50] and absorbed water[51]. After successful covalent
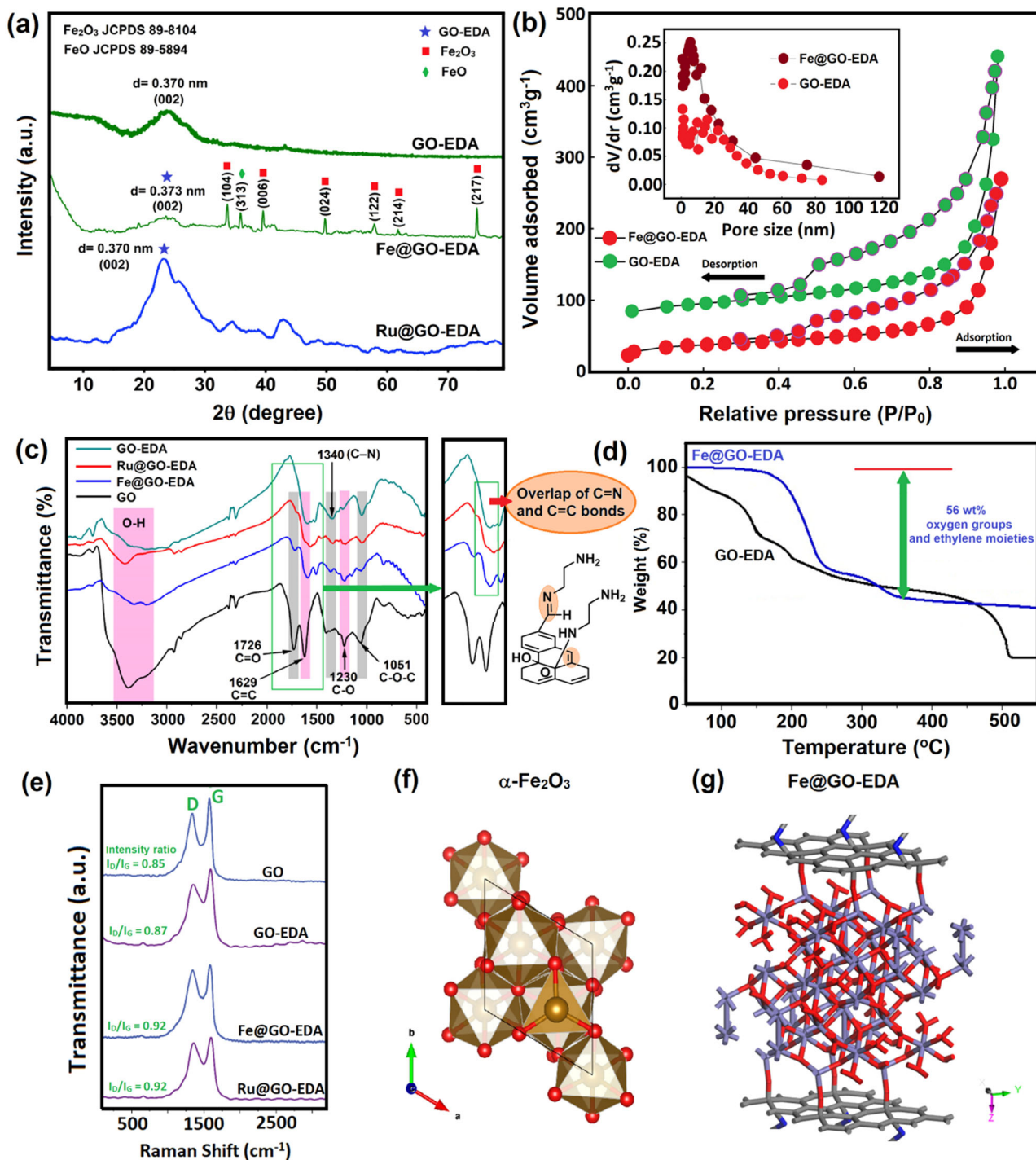
Fig. 3 | Structural characterizations of graphene oxide-based materials. a PXRD patterns of GO-EDA, Fe@GO-EDA and Ru@GO-EDA. **b** N$_2$ sorption isotherms of GO-EDA and Fe@GO-EDA at 77 K (inset: pore-size distribution profile, calculated by using BJH (Barrett–Joyner–Halenda) method). **c** FT-IR spectra of GO, GO-EDA, Fe@GO-EDA and Ru@GO-EDA. **d** TGA of GO-EDA and Fe@GO-EDA. **e** Raman spectra of GO, GO-EDA, Fe@GO-EDA and Ru@GO-EDA. **f, g** The structural modeling of α-Fe$_2$O$_3$ and Fe@GO-EDA with the help of the Materials Studio program.

functionalization of GO with reactive EDA, we detect a visible broad peak at higher 2θ values (2θ = 23.8°)[52]. The EDA-functionalized GO exhibits a broad peak caused by the (002) plane, suggesting an amorphous nature, which strongly reveals the reduction of oxygen in the functional groups (partially reduced GO by ethylenediamine) and confirms that GO-EDA has a lesser interlayer spacing of about 0.370 nm (d$_{002}$) than the synthesized GO (0.817 nm) (Fig. 3a, Supplementary Fig. 2); about fairly close to graphite.

In the case of Fe@GO-EDA, with a calculated interlayer separation of about 0.373 nm, the observed broad peak of very low intensity, induced by

the (002) plane, indicates the existence of π–π stacking (Fig. 3a). Based on this outcome, we can reasonably conclude that there must be the π–π stacking (perhaps to a lesser degree) and the conjugation of sp^2 regions in the cross-linking areas after metal decoration and lower intensity of the broad peak may be due to structural failures and collapses after immobilization of iron and/or high amount of Fe species present in the Fe-based functionalized GO (notably, another contributor may be the low dispersion). The diffraction peaks located at around 33.28, 39.81, 49.53, 57.41, 62.07, 74.70 and 79.66° correspond to the (104), (006), (024), (122), (214), and (217)

planes of rhombohedral Fe_2O_3. Based on the recorded PXRD pattern, the structural modeling of a primitive rhombohedral cell of α-Fe_2O_3 is conducted with the help of the Materials Studio program (Fig. 3f). The experimentally observed pattern by the standard JCPDS 89-8104. The peak located at around 35.94° is related to the (313) plane of tetragonal FeO, which agrees with the standard JCPDS 89-5894. Rhombohedral Fe_2O_3 is considered for the structural modeling of the Fe-based functionalized GO (Fig. 3g) and furthermore, density-functional theory (DFT) calculations are carried out using this optimized model (i.e. Fe_2O_3-loaded functionalized GO) for a better clarification. Theoretical pattern calculated from this model accords well with the experimental pattern.

Similarly, in the case of Ru@GO-EDA, a visible broad peak located at $2\theta = 23.8°$ reveals that the π–π stacking and the conjugation of sp^2 regions were restored in the cross-linking areas during the stitching of graphene sheets[53]. In sharp contrast, no prominent Ru/RuO_2 species peaks can be detected over the Ru@GO-EDA, which can possibly be due to the high dispersion or low amount of Ru species present in the Ru-based functionalized GO (Fig. 3a). In GO-EDA, the EDA molecules function as a surface modifier. The experimentally observed PXRD pattern of the synthesized GO-EDA is in good agreement with the TEM and XPS measurements (Supplementary Figs. 3 and 5), further demonstrating the generation of the stitched layered graphene sheets[49].

The porous properties of the GO-EDA and Fe@GO-EDA are assessed by N_2 adsorption isotherms measured at 77 K. The GO-EDA and Fe@GO-EDA display a typical Type-IV behavior with a hysteresis loop, reflecting their dominating mesoporous character, guest-accessible BET surface area (S_{BET}) of about 272 and 131 $m^2 g^{-1}$, respectively, and pore volume of 0.274 and 0.211 $cm^3 g^{-1}$ (Fig. 3b). Figure 3b (inset) presents the pore-size distribution calculated using BJH (Barrett–Joyner–Halenda) method that confirmed the presence of a well-organized structure of GO-EDA. The FT-IR spectra of GO, GO-EDA, Fe@GO-EDA and Ru@GO-EDA are represented in Fig. 3c.

For GO, we detect visible characteristic peaks at 1726 cm^{-1} (assigned to C=O stretching vibration present in carboxylic acid), 1629 cm^{-1} (assigned to C=C stretching vibration in aromatic ring), 1230 cm^{-1} (related to C–O–C present in epoxy groups) and 1051 cm^{-1} (assigned to C–O stretching vibration in epoxy functional groups)[54]. More intriguingly, in the case of GO, the hump-shaped band appears at around 3420 cm^{-1}, which can be due to O–H stretching vibration present in the carboxylic groups. After the successful functionalization of GO with EDA molecules, this peak is shifted to 3401 cm^{-1}, which may be due to the generation of amide groups (O=C–NH) and the exclusion of O–H groups from the carboxylic acid. The new band located at around 1635 cm^{-1} can be due to the overlap of C=N and C=C bonds. The generation of the peak for C–N vibration (1340 cm^{-1}) along with a much weaker peak for C=O stretching vibration, strongly confirms the successful covalent immobilization of ethylenediamine on GO sheets.

The thermal stability of the functionalized materials (GO-EDA and Fe@GO-EDA) is assessed by thermogravimetric analysis (TGA) at the temperature range 30–900 °C (Fig. 3d), which reveals that GO-EDA is thermally stable up to 150 °C (Fig. 3d), in contrast, the Fe@GO-EDA has good thermal stability up to 230 °C (Fig. 3d). Raman spectra of GO, GO-EDA, Fe@GO-EDA and Ru@GO-EDA are shown in Fig. 3e. It should be noted that when metals are immobilized on the GO, the intensity ratio of D and G band (i.e. I_D/I_G) usually increases, which can be caused by electronic interaction between the functionalized GO and metals (i.e. Fe or Ru species). ICP-AES experiments are used to determine metal content % of iron and ruthenium in Fe@GO-EDA and Ru@GO-EDA. Fe and Ru contents are about 3.81 and 4.12 wt% in the fresh Fe@GO-EDA and Ru@GO-EDA, respectively. We check metal content % of Fe in the recovered catalyst after the first cycle (3.77 wt%) and fifth cycle (3.76 wt%).

Transmission electron microscopy (TEM) and scanning electron microscopy (SEM) suggest the morphological features of the synthesized GO-EDA, Fe@GO-EDA and Ru@GO-EDA. To determine the structural features, morphological (internal morphology), and topographical information of these materials, we employ high-resolution transmission electron

microscopy (HR-TEM) after the treatment of ultrasonic stripping, which reveals the formation of layered materials. As shown in Fig. 4a–f, Fe@GO-EDA displays a sheet-like morphology, in which the thickness of the sheets ranges from 10 to 20 µm, and the TEM images further confirm this sheet-like morphology of Fe@GO-EDA (Fig. 4g, h). The HR-TEM image (Fig. 4h) reveals that the GO layers stack on top of each other, and these sheets are linked via π–π stacking to form a 2D-layered network. Notably, the selected area electron diffraction (SAED) pattern (Fig. 4g, inset), having visible electron-diffraction spots, suggests the presence of the GO, supporting the experimental PXRD data. SEM and TEM analyses display that the α-Fe_2O_3 has nanorods in shape (Fig. 4b–f), suggesting the successful decoration of Fe species on the functionalized GO.

The energy-dispersive spectrometer (EDS) mapping illustrates the uniform distributions of C, N, O and Fe in Fe@GO-EDA (Fig. 4k–o). As shown in Fig. 5a–f, Ru@GO-EDA displays a sheet-like morphology, in which the thickness of the sheets ranges from 0.8 to 1.5 µm, and the TEM images further confirm this sheet-like morphology of Ru@GO-EDA (Fig. 5g, h). As noticed from a magnified view (Fig. 5i), the distance between two yellow lines suggests the interplanar distance of the (211) plane for RuO_2 and the (101) plane for metallic Ru. Furthermore, the energy-dispersive spectrometer (EDS) mapping illustrates the uniform distributions of C, N, O and Ru in Ru@GO-EDA, as shown in Fig. 5l–p.

X-ray photoelectron spectroscopy (XPS) allows the elucidation of the surface properties and the interaction between the constituted components in the functionalized GO materials. The XPS full-scan survey analysis supports all comprised elements, i.e., C, N, O, Fe and Ru in Fe@GO-EDA and Ru@GO-EDA (Fig. 6a, e). The XPS C1s spectrum of Fe@GO-EDA (Fig. 6b) can be well deconvoluted into five components at 284.5 eV (assigned to the C=C and C–C bonds), 285.6 eV (assigned to the C–N and C–O bonds), 286.9 eV (assigned to C–O–C in epoxide), and 287.3 eV (assigned to the C=O in carboxyl functional groups)[55]. Moreover, the high-resolution XPS N1s spectrum of Fe@GO-EDA exhibits two subpeaks with binding energies of 398.1 and 399.5 eV (Fig. 6c). The peak at 398.1 eV is assigned to N–Fe interaction[56], whereas the peak at 399.5 eV is ascribed to C–N bonds. The XPS O1s spectrum of Fe@GO-EDA exhibits two peaks centered at 532.8 (assigned to C–O) and 531.5 eV (assigned to C=O), as illustrated in Fig. 6d. In the case of Ru@GO-EDA, the C 1s spectra overlap with Ru 3d spectra (Fig. 6f), displaying four main subpeaks located at 288.3, 287.3, 286.2 and 284.4 eV corresponding to O–C=O, C=O, C–O/C–N and adventitious C–C bond, respectively. The signals positioned at 280.6 and 282 eV correspond to Ru^0 and RuO_2, respectively[57].

Moreover, the high-resolution XPS N1s spectrum of Ru@GO-EDA exhibits two subpeaks with binding energies of 397.9 and 399.7 eV (Fig. 6g). The peak at 397.9 eV is assigned to N–Ru interaction. In the case of Fe@GO-EDA, we characterize the supported Fe_2O_3 by a spin-coupled doublet for curve fitting of $Fe2p_{3/2}$ and $Fe2p_{1/2}$ at 714.3 and 727.8 eV, respectively. We characterize the supported FeO by a spin-coupled doublet for curve fitting of $Fe2p_{3/2}$ and $Fe2p_{1/2}$ at 711 and 724.3 eV, respectively, which strongly suggests that both Fe^{2+} and Fe^{3+} species are present in the Fe@GO-EDA[58]. To unravel the coexistence of Ru and RuO_2, we further analyze the Ru species by employing XPS (Fig. 6j). The peaks located at 461.0 and 483.8 eV are assigned to metallic Ru, while those at 463.8 and 486.7 eV are related to RuO_2[59]. Further characterization of the synthesized GO-based materials and recovered catalyst supports our conclusions (Supplementary Figs. 2–11).

Reaction development and scope

After completing the characterization of Fe@GO-EDA, we examined its catalytic activity for converting methanol (**1a**) to dimethoxymethane (DMM, **2a**), as shown in Table 1. At the outset, we test Fe@GO-EDA for a model reductive functionalization of CO_2 using methanol **1a** as a model substrate and $PhSiH_3$ as a reductant under base- and solvent-free conditions (Table 1), which, to our delight, delivers 79% NMR yield of DMM in 24 h at 60 °C in the presence of 4.5 equivalent of $PhSiH_3$ (relative to **1a**) (entry 1). To further enhance the yield, we conduct the reaction in aprotic polar solvents such as CH_3CN or DMSO (deuterated). The yields are comparable under
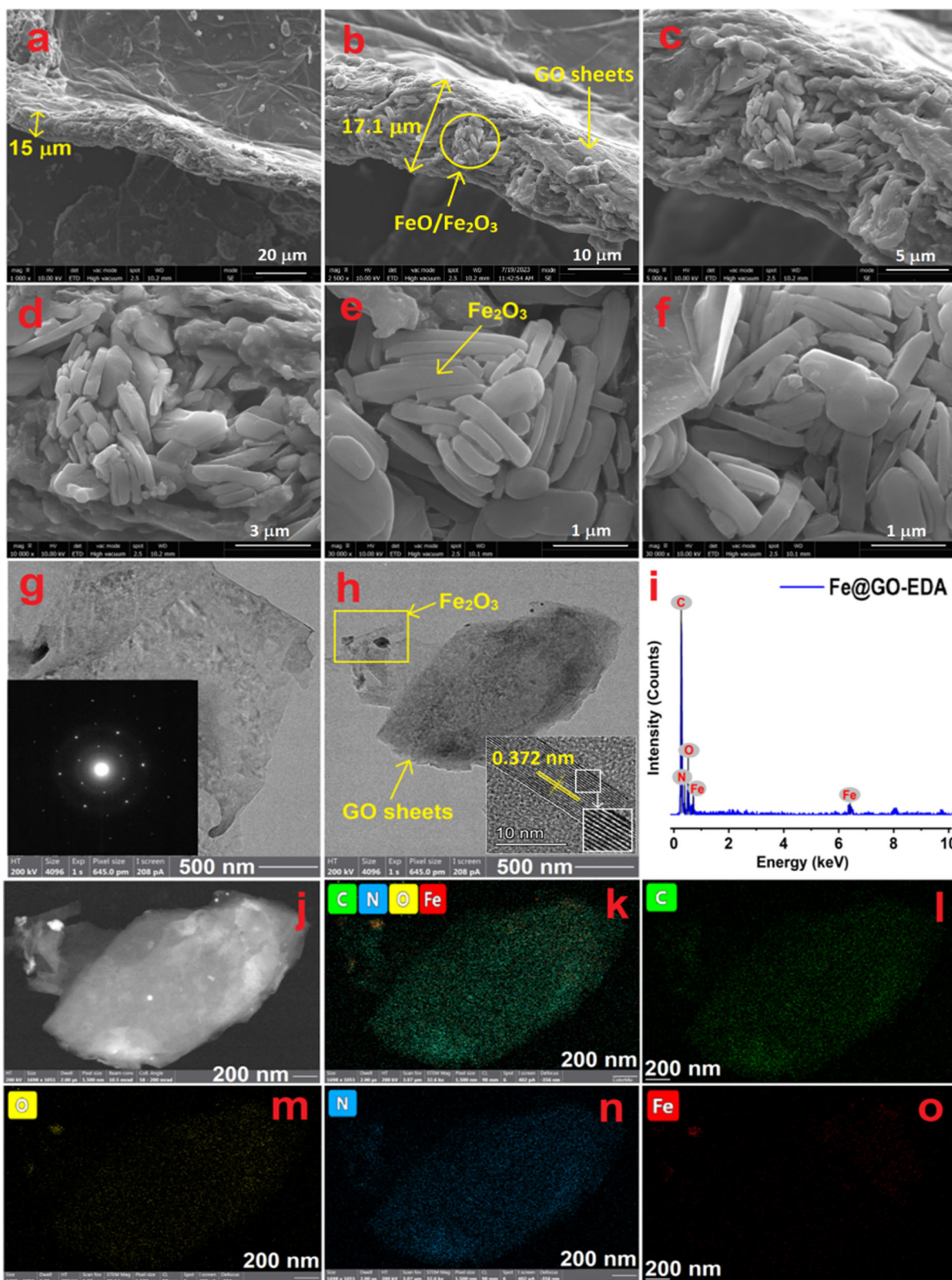
Fig. 4 | Structural characterizations of Fe@GO-EDA. a–f SEM images of Fe@GO-EDA. **g**, **h** TEM images of Fe@GO-EDA, inset **g**: SAED pattern of Fe@GO-EDA. **i** EDX of Fe@GO-EDA. **j** Electron image of Fe@GO-EDA. **k** Elemental mapping of Fe@GO-EDA for **l** carbon, **m** oxygen, **n** nitrogen and **o** iron.

solvent-free conditions (entries 2 and 3). A quick survey of non-polar solvents like benzene (deuterated) provides DMM in moderate yield (entry 4). The reaction temperature affects the catalytic outcome of CO_2 into DMM; a higher temperature of 25–90 °C appears to impart a favorable effect on the catalytic outcome, affording **2a** in good yields (entries 5–7).

Additional experiments reveal that 10 mg catalyst is required (entries 8, 9). We next screen various hydrosilane reductants; among them, $PhSiH_3$ is the most effective reductant (entries 10, 11). Finally, we examine the reaction time, and the results suggest that 36 h is required to achieve the higher conversion of CO_2 (entries 12–14). We conduct a series of control
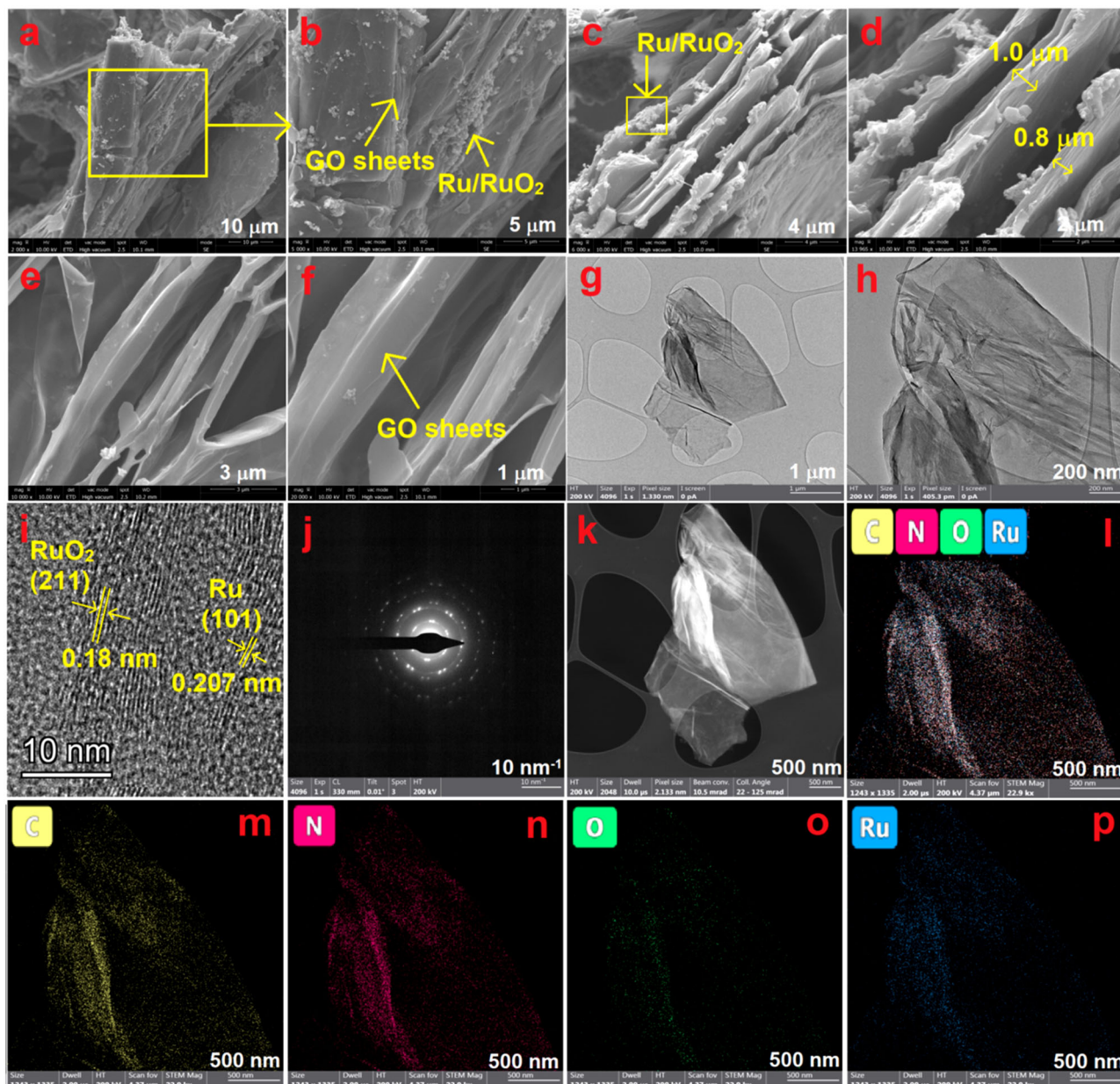
Fig. 5 | Structural characterizations of Ru@GO-EDA. a–f SEM images of Ru@GO-EDA. **g, h** TEM images of Ru@GO-EDA. **i** Magnified view where the distance between two yellow lines suggests the interplanar distance of the (211) plane for RuO$_2$ and (101) plane for metallic Ru. **j** SAED pattern of Ru@GO-EDA. **k** Electron image of Ru@GO-EDA. **l** Elemental mapping of Ru@GO-EDA for **m** carbon, **n** nitrogen, **o** oxygen and **p** ruthenium.

experiments with GO or GO-EDA as catalysts. As expected, the GO or GO-EDA do not provide the desired product DMM **2a** or methylformate (MF, **2a′**) under atmospheric CO$_2$ pressure (entries 15, 16). To further enhance the yield, we carry out the reaction in the presence of catalytic Ru@GO-EDA, however the yields are comparable under solvent-free conditions (entry 18).

Most importantly, iron is highly sustainable and environmentally friendly. Iron is one of the most recycled metals and typically produces the same quality product after recycling. Therefore, we thus expand the scope of this methodology to other substrate classes with our optimal sustainable metal-based catalyst (i.e. Fe@GO-EDA). Notably, an additional control experiment without Fe@GO-EDA or Ru@GO-EDA demonstrates no formation of DMM under the standard conditions (entry 17). Among various silanes, PhSiH$_3$ (the most typical primary silane) is most effective (entry 1). We examine a series of silanes, and alkyl silane or alkoxysilane such as diethylsilane, triethylsilane, methyldiethoxysilane,

trimethoxysilane or triethoxysilane is found to be inactive for the reaction (entries 19–23). Intriguingly, siloxane such as poly(methylhydrosiloxane) or 1,1,3,3-tetramethyldisiloxane is noted to be suitable for this transformation, affording the corresponding product in low-to-moderate yield (entries 11 and 24).

Further, to check the catalyst reusability, we recover the employed Fe@GO-EDA catalyst from the reaction mixture via centrifugation, followed by washing with organic solvents and drying in vacuo. It should be noted that the present Fe@GO-EDA can be reused at least five times (Fig. 7b), and the PXRD pattern of the recovered catalyst supports the retention of its original structural Integrity (Supplementary Fig. 9). Pore blockage after fifth run, reducing the active-site accessibility, are thought to account for the apparent loss of its catalytic activity. Additionally, structure collapse (another possible contributor to the declined activity) does not happen, as confirmed from the PXRD pattern of the recovered catalyst. Next, TEM and SEM suggest the morphological features of the recovered
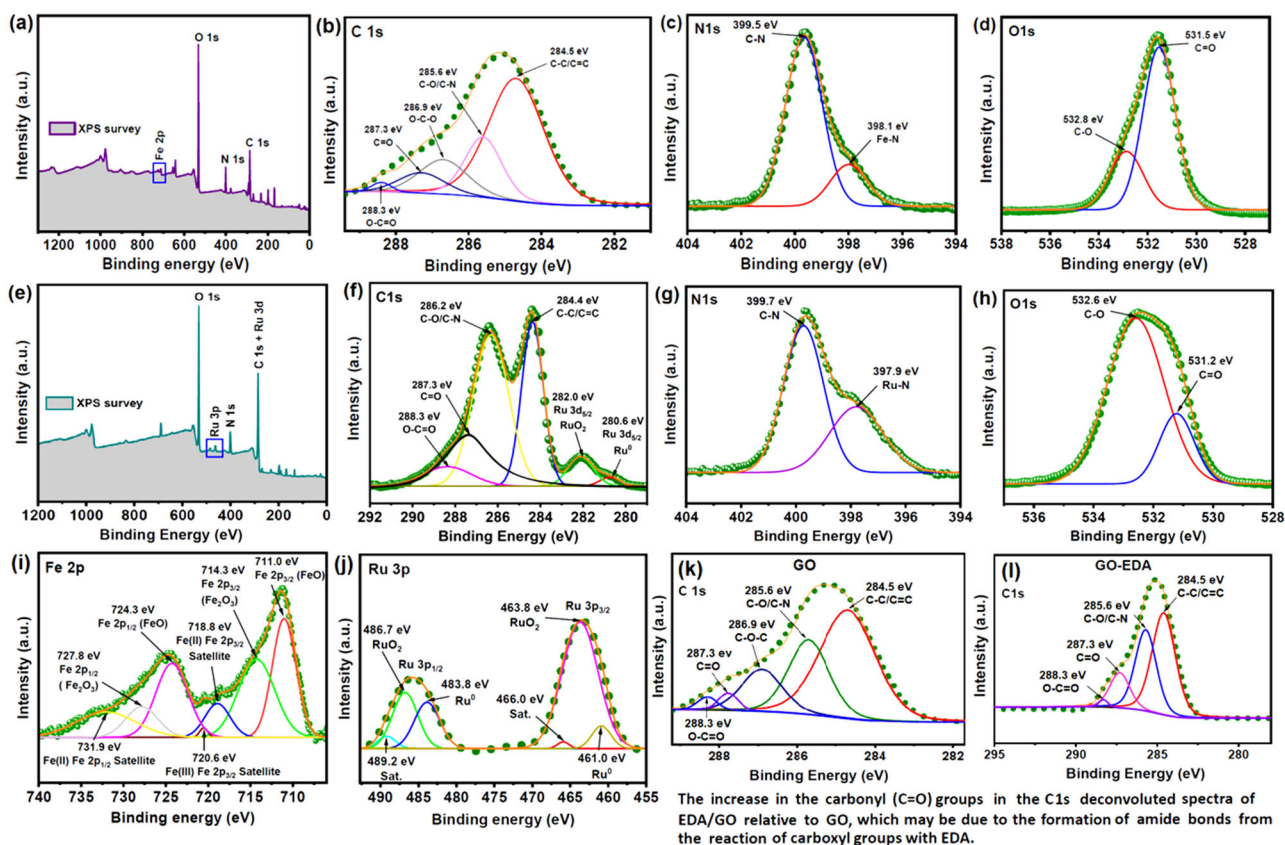
Fig. 6 | XPS spectra of graphene oxide-based materials. a XPS full-scan survey analysis of Fe@GO-EDA. The deconvoluted XPS spectra of **b** C1s (Fe@GO-EDA), **c** N1s (Fe@GO-EDA), **d** O1s (Fe@GO-EDA). **e** XPS full-scan survey analysis of Ru@GO-EDA. The deconvoluted XPS spectra of **f** C1s (Ru@GO-EDA), **g** N1s (Ru@GO-EDA) and **h** O1s (Ru@GO-EDA). The deconvoluted XPS spectra of **i** Fe 2p (Fe@GO-EDA) and **j** Ru 3p (Ru@GO-EDA). The deconvoluted XPS spectra of **k** C1s (GO) and **l** C1s (GO-EDA).

Fe@GO-EDA. TEM images of the recovered catalytic system, as presented in Supplementary Fig. 11 confirm that the morphology of recovered Fe@GO-EDA remains the same as that of the fresh catalytic system. The same can be inferred from the SEM image (Supplementary Fig. 10) of the reused catalyst after the fifth run, consistent with the PXRD pattern of the reused catalytic system (Supplementary Fig. 9). Additionally, we examine the conversion rates for the coupling reaction with time in the presence of Fe@GO-EDA catalyst, and based on the outcome obtained, the kinetic curve (Supplementary Fig. 99a) is drawn. We use methanol as an alcohol starting material for DMM synthesis under optimized reaction conditions. Additionally, we examine the conversion rates of different recycling runs for selective reductive conversion of CO_2 to DMM (Supplementary Fig. 99b).
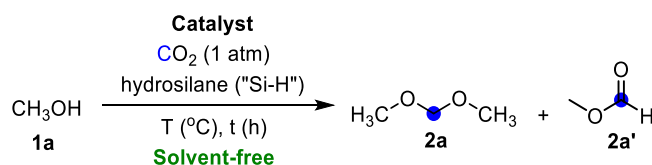
We perform hot filtration test to check the potential leaching of Fe from Fe@GO-EDA catalyst. To examine the heterogeneous nature of Fe@GO-EDA, we conducted a hot filtration experiment followed by a leaching test. The dispersed catalytic system is recovered from the reaction mixture after 12 h, and the reaction is continued with the filtrate for another 12 h at 60 °C. After a 12 h reaction time, the morpholine conversion was 73%, which changed only very little to 74% after another 12 h reaction time. The morpholine conversion is calculated by ^{1}H NMR spectroscopy of the crude reaction mixture using anisole as an internal standard. Further, we determine the Fe content in the filtrate using the atomic absorption spectroscopic (AAS) technique, which confirms that no detectable Fe is present in the filtrate. This outcome confirms no leaching of Fe from the surface of Fe@GO-EDA catalytic system during the reaction.

With the optimized reaction conditions in hand, we expand this methodology's scope to other substrate classes and summarize the obtained results in Table 2 (for NMR spectra see Supplementary Figs. 13–37). Diverse alcohols provide the desired dialkoxymethanes (DAM) in 78–99% yields

(2a–g). Using methanol in the reaction yields dimethoxymethane (DMM) with good yield of 79% (2a). However, in the presence of ethanol and *n*-propanol, the reaction affords the corresponding products in relatively higher yields (2b and 2d, 69–99%) in line with the higher boiling points of these alcohols, which are related to the chain lengths of the alcohols. We observe the catalytic coupling for aromatic alcohols such as benzyl alcohol (92%, 2g). Interestingly, cyclic secondary aliphatic alcohols such as cyclohexanol are compatible with the present methodology, yielding the desired products in good yield (78%, 2f). Notably, isopropyl alcohol is also a suitable substrate and readily converted into the corresponding product in moderate yield (55%, 2c).

We extend this approach to couplings between amines or amides employing CO_2 and PhSiH$_3$ (for NMR spectra see Supplementary Figs. 38–52). The four-electron reduction of CO_2 in the presence of secondary amines affords aminals (for example, 2i and 2j). One morpholine unit is coupled with another unit, delivering the desired aminal product (2i) in excellent yield (99%). However, pyrrolidine provides the corresponding aminal (2j) in excellent yield (99%) via the cleavage of four C–O bonds in CO_2 molecule, whereas diethylamine (1h) is noted to be completely unreactive under the optimized conditions. It should be noted that diethylamine (1h) is mono-formylated very poorly, as evidenced by NMR analysis of the crude reaction mixture. The coupling of amides using CO_2 is relatively more complex than amines as amides with pKa ~ −0.5 are less nucleophilic because of the conjugation of nitrogen lone pair with the carbonyl group in amide[60].

To our delight, the *γ*-lactam (cyclic amide) affords the corresponding CH$_2$-bridged product (2k) in 76% isolated yield without forming any byproduct, such as the complementary N-formylated product. More intriguingly, we employ the metal active site of the Fe@GO-EDA in

Table 1 | Fe@GO-EDA-catalyzed synthesis of DMM using CO_2 and hydrosilane[a]

$$CH_3OH \xrightarrow[\substack{\text{Catalyst} \\ CO_2\ (1\ \text{atm}) \\ \text{hydrosilane ("Si-H")} \\ T\ (^\circ C),\ t\ (h) \\ \text{Solvent-free}}]{} H_3C{-}O{-}O{-}CH_3 + {\rm 2a'}$$

Entry	Catalyst	Cat. amount (mg)	Si–H	Solvent	Temp. (°C)	Time (h)	Conversion[b]	2a Yield (%)[b]	2a′
1	Fe@GO-EDA	10	PhSiH$_3$	–	60	24	86	79	0
2	Fe@GO-EDA	10	PhSiH$_3$	CD$_3$CN	60	24	76	72	0
3	Fe@GO-EDA	10	PhSiH$_3$	DMSO-d_6	60	24	85	80	0
4	Fe@GO-EDA	10	PhSiH$_3$	C$_6$D$_6$	60	24	57	51	0
5	Fe@GO-EDA	10	PhSiH$_3$	–	25	24	16	12	0
6	Fe@GO-EDA	10	PhSiH$_3$	–	40	24	51	46	0
7	Fe@GO-EDA	10	PhSiH$_3$	–	90	24	77	71	0
8	Fe@GO-EDA	5	PhSiH$_3$	–	60	24	46	41	0
9	Fe@GO-EDA	15	PhSiH$_3$	–	60	24	86	79	0
10	Fe@GO-EDA	10	Ph$_2$SiH$_2$	–	60	24	58	52	0
11	Fe@GO-EDA	10	PMHS	–	60	24	67	61	0
12	Fe@GO-EDA	10	PhSiH$_3$	–	60	6	59	54	0
13	Fe@GO-EDA	10	PhSiH$_3$	–	60	12	69	63	0
14	Fe@GO-EDA	10	PhSiH$_3$	–	60	36	88	80	0
15	GO	10	PhSiH$_3$	–	60	24	0	–	–
16	GO-EDA	10	PhSiH$_3$	–	60	24	0	–	–
17	–	10	PhSiH$_3$	–	60	24	0	–	–
18	Ru@GO-EDA	10	PhSiH$_3$	–	60	24	91	86	0
19	Fe@GO-EDA	10	Et$_2$SiH$_2$	–	60	24	0	–	–
20	Fe@GO-EDA	10	Et$_3$SiH	–	60	24	0	–	–
21	Fe@GO-EDA	10	(MeO)$_3$SiH	–	60	24	0	–	–
22	Fe@GO-EDA	10	(EtO)$_3$SiH	–	60	24	0	–	–
23	Fe@GO-EDA	10	(EtO)$_2$MeSiH	–	60	24	0	–	–
24	Fe@GO-EDA	10	(Me$_2$SiH)$_2$O	–	60	24	47	42	0

[a]Reaction conditions: catalyst (Fe@GO-EDA or Ru@GO-EDA), **1a** (2 mmol), hydrosilane (9 mmol, 4.5 equiv. of "Si–H" relative to **1a**).
[b]The conversions and yields are determined by ^{1}H NMR spectroscopy of the crude reaction mixture using anisole as an internal standard.

designing sustainable transformations using in situ generated CO_2 in the coupling of inert primary amides (for example, **1l**). We attempt the coupling reaction with CO_2 using phenol and aniline as starting materials under the optimized reaction conditions. It is worth mentioning that both of them are completely unreactive under the optimized reaction conditions. We successfully identify and characterize the CH$_2$-bridged products by conducting GC–MS analysis (Supplementary Figs. 78–89). Notably, we perform ^{1}H NMR kinetic experiments for the coupling of piperidine using CO_2 (Supplementary Fig. 12).

Under the optimized reaction conditions, we examine the scope of the present coupling reaction with various long-chain alcohols (Table 3, for NMR spectra see Supplementary Figs. 53–65). The steric hindrance of long-chain aliphatic primary alcohols should be mentioned. The steric hindrance of long-chain aliphatic primary alcohols affects the coupling reaction and affords the desired products in lower yields. Citronellol (**3a**), geraniol (**3b**), phytol (**3c**), geranylgeraniol (**3d**) and solanesol (**3e**) are long-chain primary alcohols. Sterically hindered alcohol substrates are less effective, delivering the corresponding CH$_2$-bridged products **4a**, **4b** and **4d** in relatively lower yields (10–81%).

Interestingly, it is known that the initial reaction rate relies on the structure of the alcohol employed. As the alcohol is more branched, it is less

accessible and less likely to bind to the active site of the catalyst. Phytol (**3c**) is a branched-chain fatty alcohol, and the special conformation of the branched phytol chain affects the coupling reaction and provides a negligible yield of the desired product (**4c**), as confirmed by ^{1}H NMR spectrum of the crude reaction mixture. Surprisingly, in the case of **3a** and **3c**, a considerable yield of the corresponding product can be achieved by extending the reaction time and heating at 120 °C (**4a**: 81% and **4c**: 66%). Geranylgeraniol (**3d**) is a valuable diterpene alcohol in which all four double bonds have E-(trans-) geometry and provide the corresponding CH$_2$-bridged compound (**4d**) in 70% isolated yield. It is worth mentioning that solanesol (**3e**) is completely unreactive under the optimized conditions due to the crowding of branched solanesol chains. The reaction rate is also dependent on the alcohol's linearity, length as well as the alcohol position. Therefore, a bulky alcohol molecule may experience steric hindrance. We can reasonably conclude from the results that less sterically hindered substrates, like geraniol, are favored over bulkier substrates.

Mechanistic investigations

To gain insights into the mechanism of the present reductive functionalization of CO_2, we design and conduct various control experiments. Understanding the mechanistic pathway of such Fe@GO-EDA-catalyzed

Fig. 7 | Optimization of hydrosilane loading and recyclability chart of Fe@GO-EDA.
a Optimization of hydrosilane loading.
b Recyclability chart of Fe@GO-EDA up to five runs for the catalytic reductive functionalization of CO_2 to dimethoxymethane (DMM) under the optimized conditions. Yield is calculated by ^1H NMR spectroscopy of the crude reaction mixture using anisole as an internal standard. Error bars indicate the standard deviation of the coupling reaction results obtained from three independent replicates.
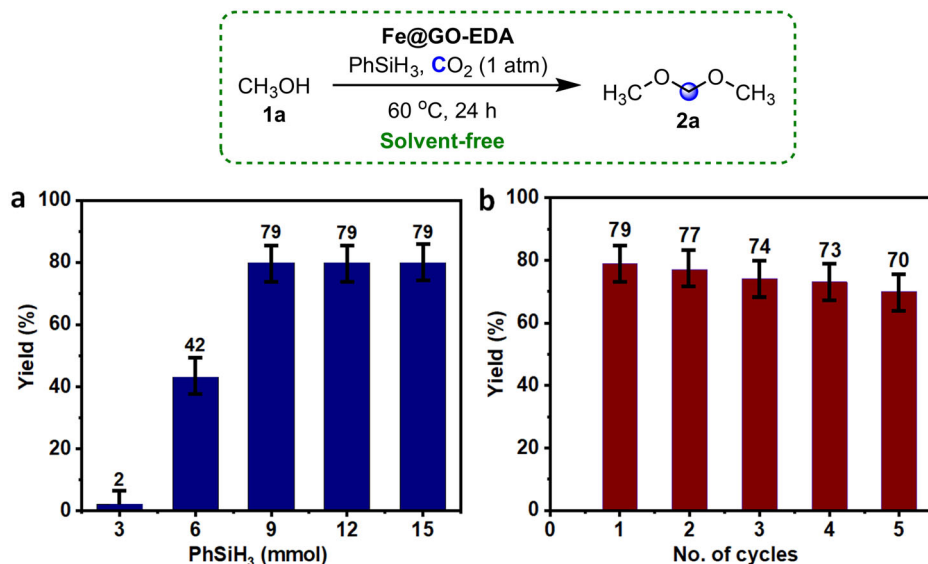
Table 2 | Fe@GO-EDA-catalyzed coupling of alcohols, amines and amides using CO_2[a]
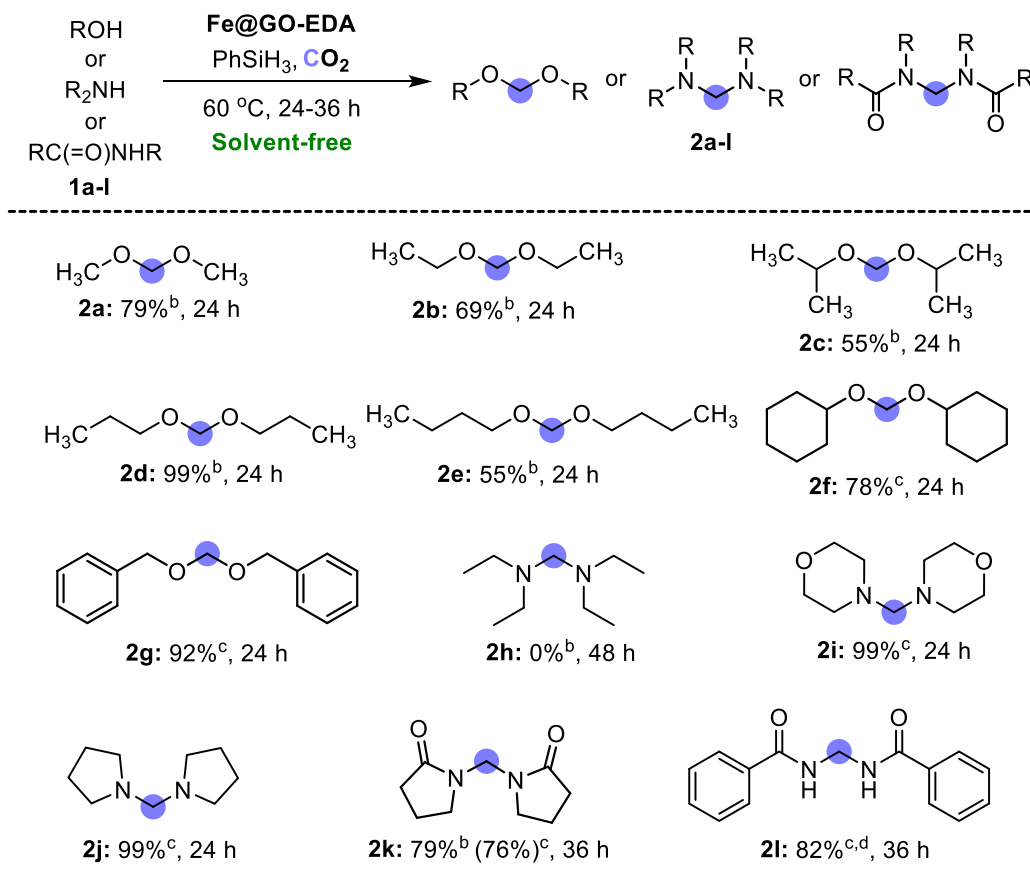
[a]Reaction conditions: Fe@GO-EDA (10 mg, 0.00682 mmol based on Fe metal), ROH/R_2NH (2 mmol), PhSiH$_3$ (9 mmol, 0.97 g, 4.5 equiv. of "Si–H" relative to alcohol or amine or amide).
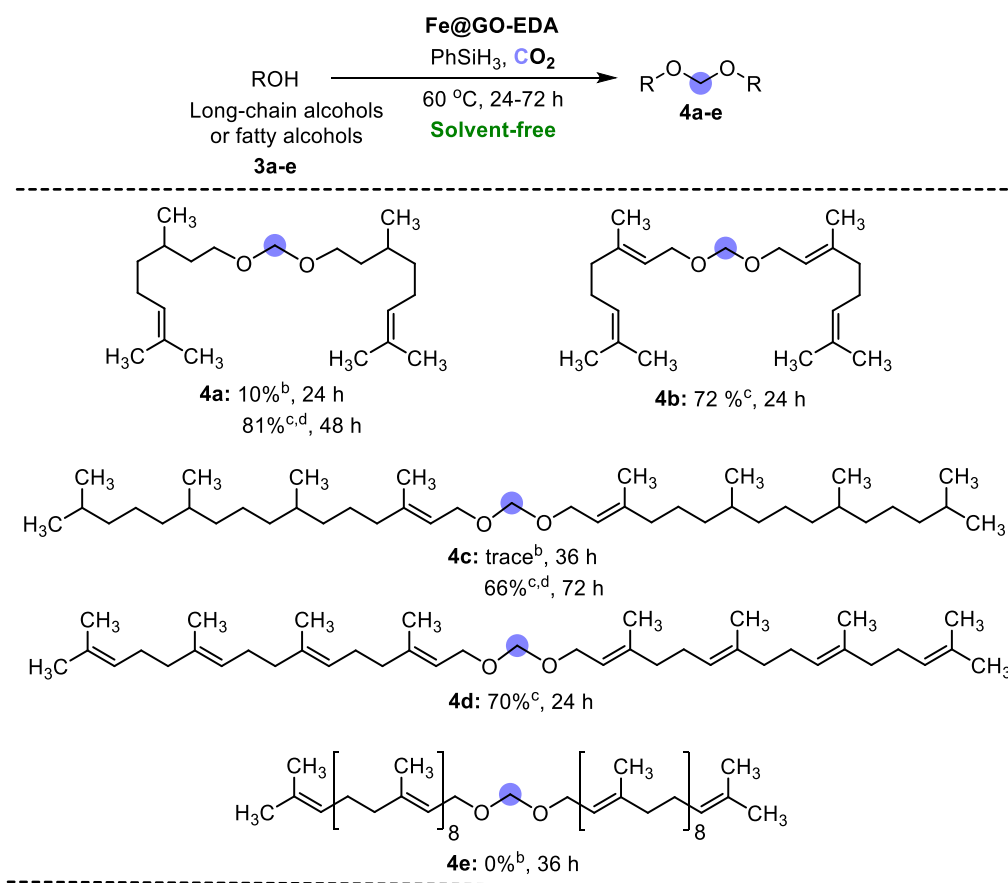[b]Yield is determined by ^1H NMR spectroscopy of the crude reaction mixture using anisole as an internal standard.
[c]Isolated yield.
[d]Performed at 120 °C.

coupling reaction is significant from potential application in designing other synthetic approaches. We further react the obtained Fe@GO-EDA with 2 equivalent Ph$_2$SiH$_2$ in CD$_3$CN in the presence of CO_2 and monitor the resulting reaction mixture by ^1H and $^{13}C\{^1H\}$ NMR spectroscopy. A singlet at $\delta = 8.17$ ppm (^1H NMR, Supplementary Fig. 66) and a peak at $\delta = 163.0$ ppm ($^{13}C\{^1H\}$ NMR, Supplementary Fig. 67) can be easily assigned to a –CHO moiety of formoxysilane (Fig. 8b) based on the literature[61–63]. Next, on adding 2.5 equiv. PhSiH$_3$ to a mixture of formoxysilane and

Table 3 | Fe@GO-EDA-catalyzed coupling of long-chain alcohols by deoxygenation of CO_2[a]

ROH
Long-chain alcohols or fatty alcohols
3a-e

→ (Fe@GO-EDA; PhSiH₃, CO_2; 60 °C, 24-72 h; Solvent-free)

R–O–CH₂–O–R
4a-e

4a: 10%[b], 24 h
81%[c,d], 48 h

4b: 72 %[c], 24 h

4c: trace[b], 36 h
66%[c,d], 72 h

4d: 70%[c], 24 h

4e: 0%[b], 36 h

[a]Reaction conditions: Fe@GO-EDA (10 mg, 0.00682 mmol based on Fe metal), ROH (2 mmol), PhSiH₃ (9 mmol, 0.97 g, 4.5 equiv. of "Si–H" relative to alcohol).

[b]Yield is determined by ¹H NMR spectroscopy of the crude reaction mixture using anisole as an internal standard.

[c]Isolated yield.

[d]Performed at 120 °C.

Fe@GO-EDA in the presence of CO_2, we detect the fading of the yellow reaction mixture into a pale-yellow solution. ¹H NMR spectroscopic study supports the presence of bis(silyl)acetal intermediate, as evident from the appearance of a resonance at $\delta = 5.14$ ppm (Supplementary Fig. 69). In the ¹³C{¹H} NMR spectrum of the reaction mixture recorded in C_6D_6 (Supplementary Fig. 70), the presence of resonance at $\delta = 84.2$ ppm can be assigned to the methylene carbon atom of bis(silyl)acetal species, revealing the formation of a critical intermediate (Fig. 8c)[64]. The existence of formoxysilane and bis(silyl)acetal species in the reaction mixture is further confirmed by ²⁹Si NMR spectroscopy (Supplementary Figs. 68 and 71).

More intriguingly, silylmethoxide competition product is formed along with the bis(silyl)acetal species (Supplementary Figs. 69 and 70). The reaction of benzamide with 1 equivalent formoxysilane at 80 °C in the presence of Fe@GO-EDA and CO_2 (1 atm) leads to the formation of N-formylbenzamide (86% isolated yield, Fig. 8d), which is confirmed by ¹H and ¹³C{¹H} NMR spectroscopy (Supplementary Figs. 94 and 95, respectively). On the other hand, no reaction occurs when we treat N-formylbenzamide with PhSiH₃ and Fe@GO-EDA in the presence of CO_2 using acetonitrile-d_3 as a solvent in the presence or absence of benzamide at 80 °C for 24 h (Fig. 8e, f).

In summary, based on various control experiments and the identification of key intermediates by NMR spectroscopic studies, the complete mechanism for the four-electron reduction of CO_2 is elucidated (Supplementary Fig. 77). Additionally, the high efficiency of our heterogeneous catalytic system (Fe@GO-EDA) can be due to the combination of the gas enrichment (or storage) effect caused by the advantageous mesopore

framework structure, which helps to increase in-pore concentrations of the substrates and the presence of several iron active sites in the heterogeneous system. Further insight into the generation of deuterated DMM was achieved from a labeling experiment employing the catalytic system Fe@GO-EDA in the presence of CD₃OD coupled with CO_2 and PhSiH₃ (Fig. 9e, for NMR spectra see Supplementary Figs. 90–93). Trapping of an important intermediate (i.e. formaldehyde) is carried out (Fig. 9c), in which 2,6-diisopropylaniline reacts with CH_2O to form the corresponding imine product, which is confirmed by ¹H and ¹³C{¹H} NMR spectroscopy (Supplementary Figs. 96 and 97, respectively). Based on this experiment, we can reasonably conclude that CH_2O unit is formed from PhSiH₃ and CO_2. Further insight into the generation of DMM is achieved from a labeling experiment employing Fe@GO-EDA in the presence of non-labeled CH₃OH in combination with ¹³CO_2 and PhSiH₃ (Supplementary Fig. 98). Intriguingly, the NMR analysis confirms the expected generation of ¹³C-labeled DMM (i.e., CH₃O¹³CH₂OCH₃). Based on this control experiment, we can conclude that the methylene carbon (–CH_2–) arises from CO_2. We conduct additional control experiments to demonstrate the mechanism further (Fig. 9).

Based on our control experiments (Figs. 8 and 9) and DFT calculations (Supplementary Figs. 72–76), we propose a mechanism as elucidated in Supplementary Fig. 77. First of all, the Si–H linkage present in PhSiH₃ is activated by Fe@GO-EDA via Fe–Si interactions, generating the active silicon species, namely, Si-1a, which is capable of delivering hydride to free CO_2 molecule, yielding the intermediate, namely, IM1a (pentavalent silicon species) via TS-1a. IM1a affords silyl formate IM1 by possible elimination of

Fig. 8 | Control experiments for the exploration of possible intermediates in four-electron reduction of CO₂. a Fe@GO-EDA-catalyzed coupling reaction of benzamide in the presence of 4.5 equiv. Ph₂SiH₂ in DMSO-d_6 to furnish the corresponding CH₂-bridged product. **b** Fe@GO-EDA-catalyzed reaction of 2 equiv. Ph₂SiH₂ and CO₂ in CD₃CN to afford formoxysilane intermediate. **c** On adding 2.5 equiv. PhSiH₃ to a mixture of formoxysilane and Fe@GO-EDA in the presence of CO₂, bis(silyl)acetal intermediate is formed. **d** The reaction of benzamide with 1 equivalent formoxysilane in the presence of Fe@GO-EDA and CO₂ leads to the formation of N-formylbenzamide. **e, f** The reaction of N-formylbenzamide with PhSiH₃ and CO₂ using Fe@GO-EDA does not occur in the presence or absence of benzamide.
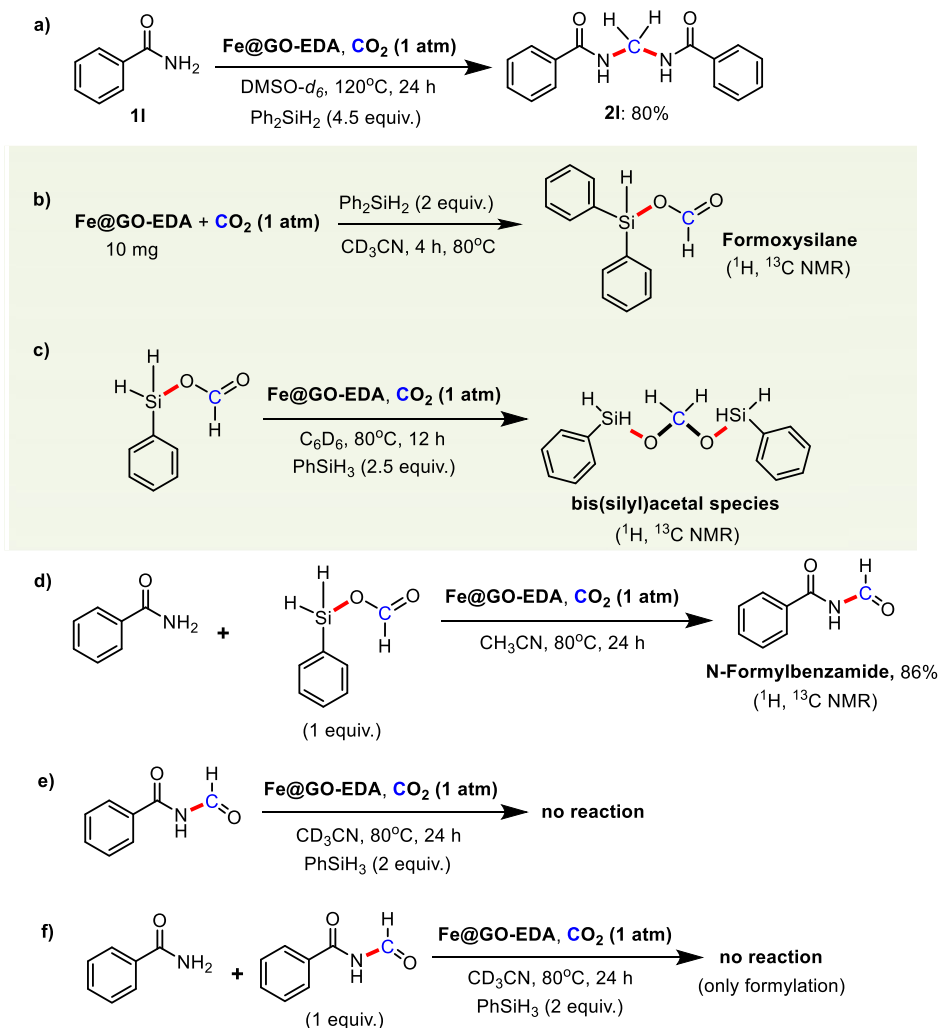
Fe@GO-EDA. In order to confirm the promoting effect of the Fe@GO-EDA catalyst, we calculate the energy of TS1 transition state for direct insertion of free CO_2 molecule in the absence of Fe@GO-EDA. The barrier of TS1 is higher as compared to that of TS-1a and TS-1b with Fe@GO-EDA-catalyzed, which strongly suggest that the Fe@GO-EDA could play pivotal role in catalyzing this process. Consequently, IM1 is reduced by Si-1a to access the C^0 intermediate, namely, bis(silyl)acetal IM2 (via IM2a), which is transformed into a significant intermediate, namely, IM3 (gaseous CH_2O) via TS3 (cyclic four-membered TS) along with possible elimination of [Si]₂O units through intramolecular cyclization and rearrangement catalyzed by Fe@GO-EDA. IM3 (formaldehyde) is attacked nucleophilically in the presence of amine (**1a**), affording an important intermediate IM4 (α-amino alcohol), which delivers another significant species IM5 (iminium intermediate) with the help of IM1. It is noteworthy to mention that IM2 is formed after elimination of Fe@GO-EDA from IM2a. Similarly, IM2a is converted into IM3 (i.e. CH_2O) via TS3a (four-membered cyclic TS), where elongation of Si–O bond facilitated by Fe@GO-EDA occurs (Si–O bond lengths extended from IM2a to TS3a, i.e. 1.8–2 Å), along with possible elimination of Fe@GO-EDA and [Si]₂O units through intramolecular cyclization and rearrangement catalyzed by Fe@GO-EDA.

In our computational study, after generating a significant gaseous intermediate IM3, the C–N linkage is generated when IM3 is attacked nucleophilically by amine and abstraction of proton from N atom of **1a** to O atom of IM3, resulting in the formation of α-amino alcohol IM4 via TS4 (a four-membered TS) with a barrier of 35.4 kcal mol⁻¹ (Fig. 10a). We showcase tandem glassware unit to produce gaseous reductant (Supplementary Fig. 1). After forming α-amino alcohol IM4, IM1′ (PhSiH₂[Fe], an activated

silane by Fe@GO-EDA) interacts with IM4, in which elongation of C–O bond present in α-amino alcohol results in the formation of an iminium cation IM5 via TS5 along with possible elimination of PhSiH₂OH and Fe@GO-EDA. Notably, the insertion of the CO_2 molecule into the Si–H linkage of Si-1a through TS1a results in PhSiH₂[Fe] (IM1′). Interestingly, if IM4 combines with a second amine unit, an energy barrier of about 47.8 kcal mol⁻¹ needs to be overcome, strongly suggesting that it is an unfeasible route for affording the desired aminal (Fig. 10e). Additionally, the C–N bond is produced in presence of water when IM3 is attacked nucleophilically by amine and abstraction of proton from N atom of **1a** to O atom of IM3, resulting in the formation of α-amino alcohol IM4 via TS4a (a six-membered TS), where H₂O plays a vital role in forming six-membered cyclic TS (i.e. TS4a), with a barrier of 21.6 kcal mol⁻¹ (Fig. 10a).

Additionally, IM5 undergoes nucleophilic addition by HCOO⁻ to access aminomethyl formate intermediate, namely, IM6. Surprisingly, the DFT calculation reveals that N-methylated product (thermodynamically more stable) could be achieved theoretically (Fig. 10a). In the whole route, the key intermediate is IM6 (aminomethyl formate) to understand aminal and methylamine production, respectively. IM6 combines with **1a** to afford aminal **1b** via four-electron reduction. It should be mentioned that transforming IM6 to the desired product **1b** is endothermic by about 0.4 kcal mol⁻¹, confirming that it is a reversible step. Furthermore, IM6 can react with PhSiH₂OH to yield the N-methylated product **1c** via *6-electron* reduction, as described in Fig. 10a, red line.

In the presence of CO_2 (1 atm), the net reaction will terminate at the C^0 level to access the desired aminal as the final product (namely, **1b**), which is kinetically stable (Fig. 10). It is reported that the aminal is achieved via two
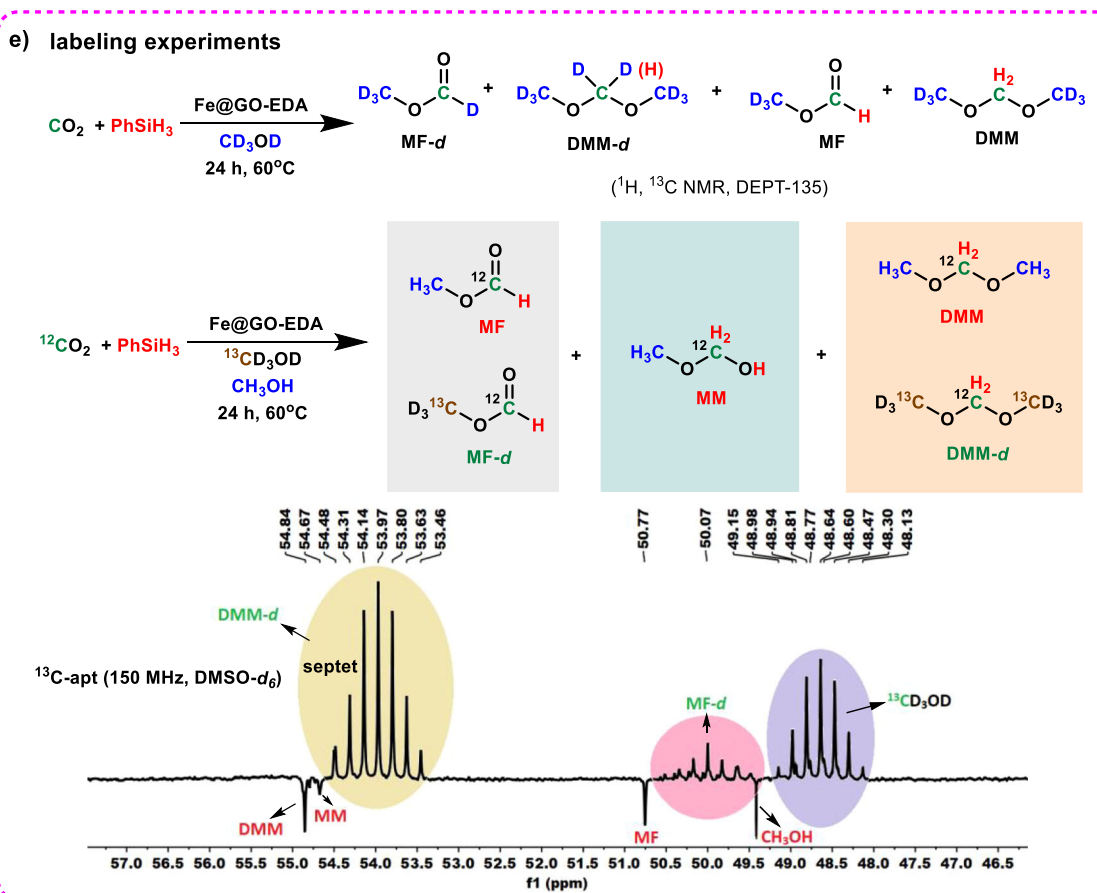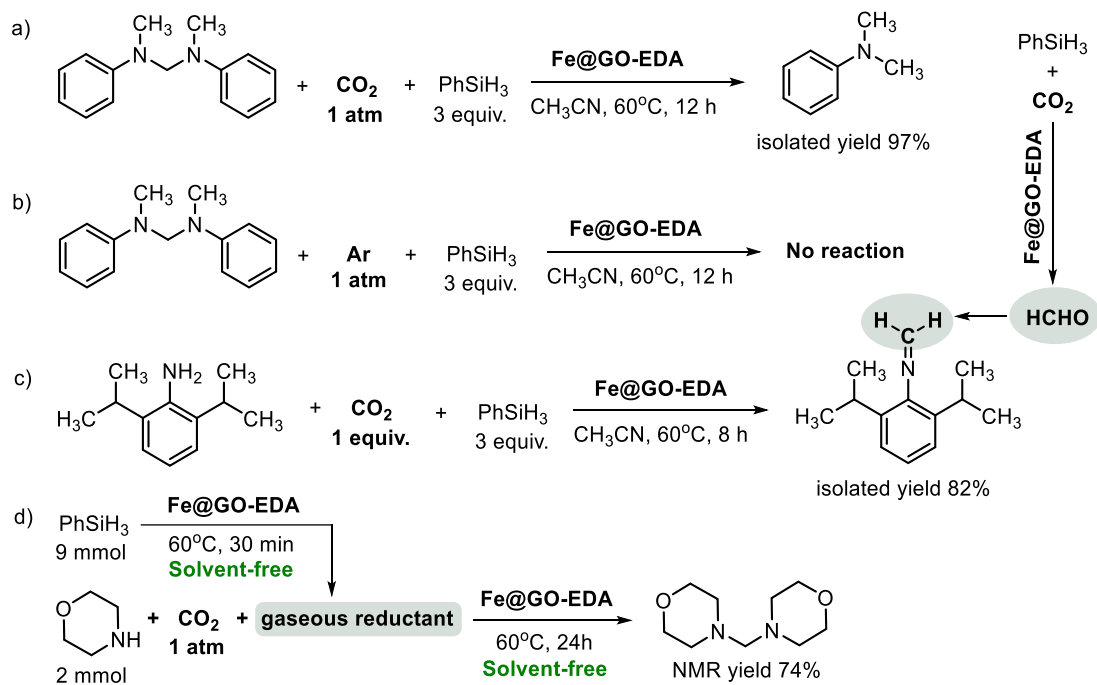
Fig. 9 | Additional control experiments for the exploration of possible intermediates in four-electron reduction of CO_2. a The reaction of aminal with CO_2 and $PhSiH_3$ in the presence of Fe@GO-EDA in CH_3CN to furnish the corresponding methylated product. **b** The reaction of aminal with $PhSiH_3$ and Ar in the presence of Fe@GO-EDA does not occur. **c** Trapping of formaldehyde intermediate is carried out, in which 2,6-diisopropylaniline reacts with CH_2O to form the corresponding imine product. **d** The reaction of morpholine with gaseous reductant and CO_2 in the presence of Fe@GO-EDA to furnish the corresponding aminal. **e** Labeling experiments employing the catalytic system Fe@GO-EDA in the presence of CD_3OD or $^{13}CD_3OD/CH_3OH$ coupled with CO_2 and $PhSiH_3$.
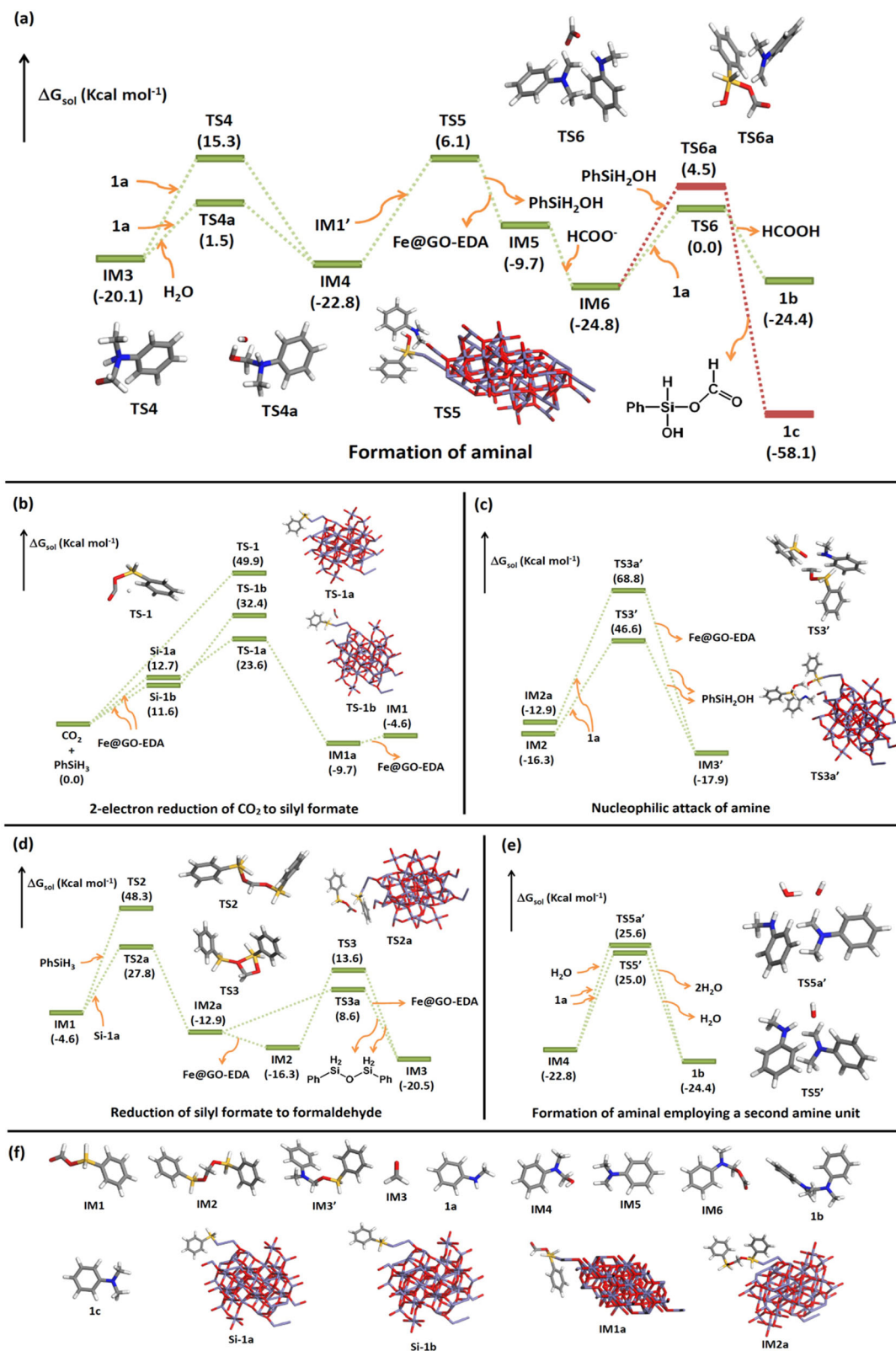
Fig. 10 | DFT-computed reaction pathways. a Potential energy surface for the formation of aminal. **b** 2-electron reduction of CO_2 to silyl formate. **c** The potential energy profile for the nucleophilic attack of amine. **d** The potential energy surface for reduction of silyl formate to formaldehyde. **e** Free energy profile for the generation of aminal employing a second amine unit. **f** Optimized structures of several intermediates. The intermediates and transition states (TS) along the reaction pathway are shown. The energy values and bond lengths given in the figure are in Kcal/mol. Color code: C (black), N (blue), H (white), Si (yellow), O (red) and Fe (violet). For clarity, GO-EDA is not shown in the rest of the panels.

successive nucleophilic attacks of the amine unit toward the C^0 intermediate, namely, bis(silyl)acetal[46,65]. Nevertheless, our computational outcomes reveal that it is an unfeasible route for affording the desired aminal (Fig. 10c). More intriguingly, Wang et al. demonstrate that formaldehyde formed from the dissociation of the C^0 intermediate is expected for the NHC-promoted transformation of CO_2 into methanol with the help of computational study[66,67]. Production of formaldehyde in our system is also validated by conducting the control experiment (Figs. 8 and 9). Consequently, an alternative mechanistic pathway via formaldehyde route seems to be more logical (Supplementary Fig. 77).

The CO_2 transformation into fuel additives, aminals, or some value-added CH_2-bridged compounds is an exceptional platform for sustainable catalysis, resulting in complete catalytic CO_2 deoxygenation. Most interestingly, it involves complete C–O bond-breaking and the generation of two C–H linkages via reduction, followed by the formation of two C–O (in the case of alcohols) or C–N (in the case of amines or amides) bonds via subsequent functionalization. Based on experimental results and theoretical investigations, a plausible mechanism is presented in Supplementary Fig. 77. However, no reaction occurs when we treat N-formylbenzamide with $PhSiH_3$ and 10 mg Fe@GO-EDA in the presence of CO_2 using acetonitrile-d_3 as a solvent in the presence or absence of benzamide at 80 °C for 24 h. Typically, researchers synthesize CH_2-bridged compounds by conducting an amine condensation reaction over paraformaldehyde, and an option for the production of CH_2-bridged compounds directly from CO_2 can depend on CO_2 hydrosilylation into a key intermediate, C^0 bis(silyl)acetal, followed by nucleophilic addition of the two amine units.

The bis(silyl)acetal having stronger electrophilicity is formed (notably, precise detection of formaldehyde), and consumption of the most nucleophilic reagent is expected to be rapid so that we can synthesize CH_2-bridged compounds with good selectivities. Following this mechanism, the reduction and functionalization steps are consecutive. Still, their relative rates play a pivotal role in ensuring the transformation of CO_2 into the desired methylene-bridged compound while avoiding by-product formation (i.e., silylmethoxide and formamide competition products).

Conclusions

We have successfully developed Fe- and Ru-decorated functionalized graphene oxide materials for the effective sustainable reductive functionalization of CO_2. These two catalysts can promote the coupling of various O–H (alcohols) and N–H (amines and amides) functionalities with CO_2 and $PhSiH_3$ under very mild conditions (solvent-free/cocatalyst-free/base-free and atmospheric pressure). Most importantly, iron is highly sustainable and environmentally friendly. Iron is one of the most recycled metals and typically produces the same quality product after recycling. Considering sustainability, we expand this methodology with an optimal eco-friendly metal-based catalyst (i.e. Fe@GO-EDA). Further, we demonstrate that the heterogenization of metal-based homogeneous catalysts can make the process sustainable, cost-effective, and environment-friendly with good recyclability. This study advances the knowledge of sustainable heterogeneous catalysis for synthesis. Further work in utility of functionalized graphene oxide as a heterogeneous catalyst for CO_2 valorization is currently ongoing in our laboratory.

Methods

All characterizations are described in detail in the Supplementary Information section (SI—"Results and discussion" section). The synthesis of the EDA-functionalized GO and the Fe- and Ru-based functionalized GO is depicted in Fig. 2. Bulk EDA-functionalized GO and 45 wt% $RuCl_3·H_2O$ are suspended in water, followed by ultra-sonication for 30 min. After that, the suspension is dried at 100 °C, calcined at 300 °C for 2 h in air, and labeled as Ru@GO-EDA. Similarly, we successfully decorate α-Fe_2O_3 nanorods with FeO on covalently functionalized GO with EDA (Fe@GO-EDA). The Fe- or Ru-based GO-EDA is found to be utterly insoluble in common organic solvents such as DMF, DMSO, acetone, toluene, CH_3CN, etc. and stable over a few months at ambient conditions, which confirms its stability in organic solvents. We characterize the Fe@GO-EDA and Ru@GO-EDA catalysts by several standard analytical techniques such as X-ray photo-electron spectroscopy (XPS), transmission electron microscopy (TEM), field emission scanning electron microscopy (FESEM), energy dispersive X-ray spectroscopy (EDS), thermogravimetric analysis (TGA), Brunauer–Emmett–Teller (BET), Fourier-transform infrared spectroscopy (FT-IR), ultraviolet–visible (UV–vis) spectroscopy etc.

Synthesis of graphene oxide (GO)

We synthesize graphene oxide by oxidation of graphite flakes (Aldrich) using the following reported method[68]. In this method, we take a 200 mL mixture of concentrated H_3PO_4 and H_2SO_4 (20 :180 v/v) in a 500 mL round bottom flask. Then, we slowly add graphite flakes (1.5 g) to the mixture. Next, we add $KMnO_4$ (9.0 g) in portions to the above mixture. After that, the above solution is continued to stir for 16 h at 50 °C. The mixture is then cooled, followed by adding 3 ml 30% H_2O_2. Subsequently, it is cooled in an ice bath for several hours until the appearance of brown coloration. The mixture is centrifuged, decanted and washed properly with hydrochloric acid solution (10%), deionized H_2O, EtOH one by one. Finally, the obtained brown graphene oxide (GO) is dried under vacuum at room temperature (Fig. 1).

Synthesis of Ru/RuO₂ decorated ethylenediamine functionalized graphene oxide (Ru@GO-EDA)

GO (1 g) is suspended in 50 ml toluene in a 100 ml conical flask and is sonicated for about 2 h. Then, we add 1.68 mmol of ethylenediamine (EDA) to the solution, which is further sonicated for 1 h. We synthesize RuO_2 and/or Ru-loaded functionalized GO via wet impregnation[69]. Typically, 200 mg bulk GO and 45 wt% $RuCl_3·H_2O$ are suspended in 40 ml water followed by ultra-sonication (Fisher brand) for 30 min. After that, the suspension was dried at 100 °C, calcined at 300 °C for 2 h in the air, and labeled as Ru@GO-EDA. The obtained material is washed several times with water to remove $RuCl_3$ residues (Fig. 1).

Synthesis of α-Fe₂O₃/FeO decorated ethylenediamine functionalized graphene oxide (Fe@GO-EDA)

We synthesize a mixture of α-Fe_2O_3 nanorods and FeO by hydrothermal method[70]. GO (1 g) is suspended in 50 ml toluene in a 100 ml conical flask and is sonicated for about 2 h. Then, we add 1.68 mmol of ethylenediamine (EDA) to the solution, which is further sonicated for 1 h. After that, we add 70 mg of α-Fe_2O_3 nanorods/FeO dropwise, and the whole mixture is stirred for 4 h. In the last step, the mixture is centrifuged, washed thoroughly with toluene, and dried under a vacuum oven at 100 °C to get Fe@GO-EDA catalyst (Fig. 1).

Data availability

All the data generated in this study are available within the main text and Supplementary Information. Data are also available from the corresponding author upon request.

References

1. Diesel, R. Method of and apparatus for converting heat into work. US patent **542**,846 (1895).
2. Gadonneix, P. et al. *Global Transport Scenarios 2050* 456 (World Energy Council, 2011).
3. Kalghatgi, G. T. The outlook for fuels for internal combustion engines. *Int. J. Engine Res.* **15**, 383–398 (2014).
4. Alagumalai, A. Internal combustion engines: progress and prospects. *Renew. Sustain. Energy Rev.* **38**, 561–571 (2014).
5. *IARC Monographs on the Evaluation of Carcinogenic Risks to Humans* 46 (International Agency for Research on Cancer: Lyon, France, 1989).

6. *Diesel Engine Exhaust Carcinogenic* 213 http://press.larc.fr/pr213_E. pdf (World Health Organization, International Agency for Research on Cancer, 2012).

7. Steiner, S., Bisig, C., Petri-Fink, A. & Rothen-Rutishauser, B. Diesel exhaust: current knowledge of adverse effects and underlying cellular mechanisms. *Arch. Toxicol.* **90**, 1541–1553 (2016).

8. Connolly, D., Mathiesen, B. V. & Ridjan, I. A comparison between renewable transport fuels that can supplement or replace biofuels in a 100% renewable energy system. *Energy* **73**, 110–125 (2014).

9. Grube, T. et al. An option for stranded renewables: electrolytic-hydrogen in future energy systems. *Sustain. Energy Fuels* **2**, 1500–1515 (2018).

10. Alanazi, F. Battery electric vehicles are an attractive option for short-distance transportation. *Appl. Sci.* **13**, 6016 (2023).

11. Ribeiro, N. M. et al. The role of additives for diesel and diesel blended (ethanol or biodiesel) fuels: a review. *Energy Fuels* **21**, 2433–2445 (2007).

12. Arcoumanis, C., Bae, C., Crookes, R. & Kinoshita, E. The potential of di-methyl ether (DME) as an alternative fuel for compression-ignition engines: a review. *Fuel* **87**, 1014–1030 (2008).

13. Zhang, G. D., Liu, H., Xia, X. X., Zhang, W. G. & Fang, J. H. Effects of dimethyl carbonate fuel additive on diesel engine performances. *Proc. Inst. Mech. Eng. D* **219**, 897–903 (2005).

14. Burger, J., Siegert, M., Ströfer, E. & Hasse, H. Poly (oxymethylene) dimethyl ethers as components of tailored diesel fuel: properties, synthesis and purification concepts. *Fuel* **89**, 3315–3319 (2010).

15. Jacob, E. & Maus, W. Oxymethylenether als potenziell CO_2-neutraler Kraftstoff für saubere Dieselmotoren Teil 2: Erfüllung des Nachhaltigkeitsanspruchs. *Motortech. Z.* **78**, 54–61 (2017).

16. Omari, A., Heuser, B. & Pischinger, S. Potential of oxymethylenether-diesel blends for ultra-low emission engines. *Fuel* **209**, 232–237 (2017).

17. Härtl, M., Gaukel, K., Pélerin, D. & Wachtmeister, G. Oxymethylenether als potenziell CO_2-neutraler Kraftstoff für saubere Dieselmotoren Teil 1: Motorenuntersuchungen. *Motortech. Z.* **78**, 52–59 (2017).

18. Deutz, S. et al. Cleaner production of cleaner fuels: wind-to-wheel–environmental assessment of CO_2-based oxymethylene ether as a drop-in fuel. *Energy Environ. Sci.* **11**, 331–343 (2018).

19. Thenert, K., Beydoun, K., Wiesenthal, J., Leitner, W. & Klankermayer, J. Ruthenium-catalyzed synthesis of dialkoxymethane ethers utilizing carbon dioxide and molecular hydrogen. *Angew. Chem. Int. Ed.* **128**, 12454–12457 (2016).

20. Siebert, M., Seibicke, M., Siegle, A. F., Kräh, S. & Trapp, O. Selective ruthenium-catalyzed transformation of carbon dioxide: an alternative approach toward formaldehyde. *J. Am. Chem. Soc.* **141**, 334–341 (2019).

21. Schieweck, B. G. & Klankermayer, J. Tailor-made molecular cobalt catalyst system for the selective transformation of carbon dioxide to dialkoxymethane ethers. *Angew. Chem.* **56**, 10854–10857 (2017).

22. Ren, J., Xin, F. & Xu, Y. A review on direct synthesis of dimethoxymethane. *Chin. J. Chem. Eng.* **50**, 43–55 (2022).

23. Ahmad, W., Chan, F. L., Hoadley, A., Wang, H. & Tanksale, A. Synthesis of oxymethylene dimethyl ethers (OMEn) via methanol mediated CO_x hydrogenation over Ru/BEA catalysts. *Appl. Catal. B* **269**, 118765 (2020).

24. Fan, Z., Guo, H., Fang, K. & Sun, Y. Efficient V_2O_5/TiO_2 composite catalysts for dimethoxymethane synthesis from methanol selective oxidation. *RSC Adv.* **5**, 24795–24802 (2015).

25. Konrath, R. et al. Performance enhancing additives for reusable ruthenium-triphos catalysts in the reduction of CO_2 to dimethoxymethane. *Green Chem.* **22**, 6464–6470 (2020).

26. Thavornprasert, K. A., Capron, M., Jalowiecki-Duhamel, L. & Dumeignil, F. One-pot 1, 1-dimethoxymethane synthesis from methanol: a promising pathway over bifunctional catalysts. *Catal. Sci. Technol.* **6**, 958–970 (2016).

27. Sun, R., Delidovich, I. & Palkovits, R. Dimethoxymethane as a cleaner synthetic fuel: synthetic methods, catalysts, and reaction mechanism. *ACS Catal.* **9**, 1298–1318 (2019).

28. Lluna-Galán, C., Izquierdo-Aranda, L., Adam, R. & Cabrero-Antonino, J. R. Catalytic reductive alcohol etherifications with carbonyl-based compounds or CO_2 and related transformations for the synthesis of ether derivatives. *ChemSusChem* **14**, 3744–3784 (2021).

29. Lautenschütz, L. et al. Physico-chemical properties and fuel characteristics of oxymethylene dialkyl ethers. *Fuel* **173**, 129–137 (2016).

30. Baranowski, C. J., Bahmanpour, A. M. & Kröcher, O. Catalytic synthesis of polyoxymethylene dimethyl ethers (OME): a review. *Appl. Catal. B* **217**, 407–420 (2017).

31. Reuss, G., Disteldorf, W., Gamer, A. O. & Hilt. A. in *Ullman's Encyclopedia of Industrial Chemistry* (Wiley-VCH, Weinheim, 2000).

32. Wang, J. et al. Method for producing polyoxymethylene dimethyl ethers. US patent US2015/0291722 (2015).

33. Wang, J. et al. Fluidized bed reactor and method for preparing polyoxymethylene dimethyl ethers from dimetroxymethane and paraformaledehyde. US patent US2015/0273426A1 (2015).

34. Li, M. et al. Ruthenium trichloride as a new catalyst for selective production of dimethoxymethane from liquid methanol with molecular oxygen as sole oxidant. *Catal. Commun.* **68**, 46–48 (2015).

35. Liu, X. F., Li, X. Y. & He, L. N. Transition metal-catalyzed reductive functionalization of CO_2. *Eur. J. Org. Chem.* **2019**, 2437–2447 (2019).

36. Liu, X. F., Li, X. Y., Qiao, C. & He, L. N. Transition-metal-free catalysis for the reductive functionalization of CO_2 with amines. *Synlett* **29**, 548–555 (2018).

37. Centi, G., Quadrelli, E. A. & Perathoner, S. Catalysis for CO_2 conversion: a key technology for rapid introduction of renewable energy in the value chain of chemical industries. *Energy Environ. Sci.* **6**, 1711–1731 (2013).

38. Klankermayer, J., Wesselbaum, S., Beydoun, K. & Leitner, W. Selective catalytic synthesis using the combination of carbon dioxide and hydrogen: catalytic chess at the interface of energy and chemistry. *Angew. Chem. Int. Ed.* **55**, 7296–7343 (2016).

39. Cabrero-Antonino, J. R., Adam, R. & Beller, M. Catalytic reductive N-alkylations using CO_2 and carboxylic acid derivatives: recent progress and developments. *Angew. Chem. Int. Ed.* **58**, 12820–12838 (2019).

40. Liu, Q., Wu, L., Jackstell, R. & Beller, M. Using carbon dioxide as a building block in organic synthesis. *Nat. Commun.* **6**, 1–15 (2015).

41. Jiang, Y., Blacque, O., Fox, T. & Berke, H. Catalytic CO_2 activation assisted by rhenium hydride/B(C_6F_5)$_3$ frustrated lewis pairs-metal hydrides functioning as FLP bases. *J. Am. Chem. Soc.* **135**, 7751–7760 (2013).

42. Ríos, P., Curado, N., López-Serrano, J. & Rodríguez, A. Selective reduction of carbon dioxide to bis(silyl)acetal catalyzed by a PBP-supported nickel complex. *Chem. Commun.* **52**, 2114–2117 (2016).

43. LeBlanc, F. A., Piers, W. E. & Parvez, M. Selective hydrosilation of CO_2 to a bis(silylacetal) using an anilido bipyridyl-ligated organoscandium catalyst. *Angew. Chem. Int. Ed.* **126**, 808–811 (2014).

44. Seibicke, M., Siebert, M., Siegle, A. F., Gutenthaler, S. M. & Trapp, O. Application of hetero-triphos ligands in the selective ruthenium-catalyzed transformation of carbon dioxide to the formaldehyde oxidation state. *Organometallics* **38**, 1809–1814 (2019).

45. Siebert, M., Krennrich, G., Seibicke, M., Siegle, A. F. & Trapp, O. Identifying high-performance catalytic conditions for carbon dioxide reduction to dimethoxymethane by multivariate modeling. *Chem. Sci.* **10**, 10466–10474 (2019).

46. Frogneux, X., Blondiaux, E., Thuéry, P. & Cantat, T. Bridging amines with CO_2: organocatalyzed reduction of CO_2 to aminals. *ACS Catal.* **5**, 3983–3987 (2015).

47. Das, A., Sarkar, P., Maji, S., Pati, S. K. & Mandal, S. K. Mesoionic N-heterocyclic imines as super nucleophiles in catalytic couplings of amides with CO_2. *Angew. Chem. Int. Ed.* **134**, e202213614 (2022).

48. Ahmad, W. et al. Dimethoxymethane production via CO_2 hydrogenation in methanol over novel Ru based hierarchical BEA. *J. Energy Chem.* **66**, 181–189 (2022).

49. Kim, N. H., Kuila, T. & Lee, J. H. Simultaneous reduction, functionalization and stitching of graphene oxide with ethylenediamine for composites application. *J. Mater. Chem. A* **1**, 1349–1358 (2013).

50. Du, M. et al. Synthesis of nitrogen-doped reduced graphene oxide directly from nitrogen-doped graphene oxide as a high-performance lithium ion battery anode. *RSC Adv.* **4**, 42412–42417 (2014).

51. Sheng, X., Cai, W., Zhong, L., Xie, D. & Zhang, X. Synthesis of functionalized graphene/polyaniline nanocomposites with effective synergistic reinforcement on anticorrosion. *Ind. Eng. Chem. Res.* **55**, 8576–8585 (2016).

52. Khan, F., Baek, S. H. & Kim, J. H. One-step and controllable bipolar doping of reduced graphene oxide using TMAH as reducing agent and doping source for field effect transistors. *Carbon* **100**, 608–616 (2016).

53. Xu, X. et al. Self-sensing, ultralight, and conductive 3D graphene/iron oxide aerogel elastomer deformable in a magnetic field. *ACS Nano* **9**, 3969–3977 (2015).

54. Singh, A., Sharma, N., Arif, M. & Katiyar, R. S. Electrically reduced graphene oxide for photovoltaic application. *J. Mater. Res.* **34**, 652–660 (2019).

55. Johra, F. T., Lee, J. W. & Jung, W. G. Facile and safe graphene preparation on solution based platform. *J. Ind. Eng. Chem.* **20**, 2883–2887 (2014).

56. Peng, H. et al. High performance Fe-and N-doped carbon catalyst with graphene structure for oxygen reduction. *Sci. Rep.* **3**, 1765 (2013).

57. Wang, H., Li, X., Ruan, Q. & Tang, J. Ru and RuO_x decorated carbon nitride for efficient ammonia photosynthesis. *Nanoscale* **12**, 12329–12335 (2020).

58. He, S. et al. Kinetics of iron removal from Ti-extraction blast furnace slag by chlorination calcination. *Open Chem.* **17**, 1146–1156 (2019).

59. Morgan, D. J. Resolving ruthenium: XPS studies of common ruthenium materials. *Surf. Interface Anal.* **47**, 1072–1079 (2015).

60. Hota, P. K., Sau, S. C. & Mandal, S. K. Metal-free catalytic formylation of amides using CO_2 under ambient conditions. *ACS Catal.* **8**, 11999–12003 (2018).

61. Sarkar, D. et al. N-heterocyclic carbene-stabilized germa-acylium ion: reactivity and utility in catalytic CO_2 functionalizations. *J. Am. Chem. Soc.* **142**, 15403–15411 (2020).

62. Riduan, S. N., Ying, J. Y. & Zhang, Y. Mechanistic insights into the reduction of carbon dioxide with silanes over N-heterocyclic carbene catalysts. *ChemCatChem* **5**, 1490–1496 (2013).

63. Motokura, K., Nakagawa, C., Pramudita, R. A. & Manaka, Y. Formate-catalyzed selective reduction of carbon dioxide to formate products using hydrosilanes. *ACS Sustain. Chem. Eng.* **7**, 11056–11061 (2019).

64. Courtemanche, M. A., Légaré, M. A., Rochette, É. & Fontaine, F. G. Phosphazenes: efficient organocatalysts for the catalytic hydrosilylation of carbon dioxide. *Chem. Commun.* **51**, 6858–6861 (2015).

65. Liu, X. F., Li, X. Y., Qiao, C., Fu, H. C. & He, L. N. Betaine catalysis for hierarchical reduction of CO_2 with amines and hydrosilane to form formamides, aminals, and methylamines. *Angew. Chem. Int. Ed.* **56**, 7425–7429 (2017).

66. Lu, Y. et al. Formylation or methylation: what determines the chemoselectivity of the reaction of amine, CO_2, and hydrosilane catalyzed by 1,3,2-diazaphospholene? *Chem. Sci.* **8**, 7637–7650 (2017).

67. Huang, F., Lu, G., Zhao, L., Li, H. & Wang, Z.-X. The catalytic role of N-heterocyclic carbene in a metal-free conversion of carbon dioxide into methanol: a computational mechanism study. *J. Am. Chem. Soc.* **132**, 12388–12396 (2010).

68. Paul, R., Gayen, R. N., Biswas, S., Bhat, S. V. & Bhunia, R. Enhanced UV detection by transparent graphene oxide/ZnO composite thin films. *RSC Adv.* **6**, 61661–61672 (2016).

69. Ye, C., Zhang, N., Wang, D. & Li, Y. Single atomic site catalysts: synthesis, characterization, and applications. *Chem. Commun.* **56**, 7687–7697 (2020).

70. Hadia, N. M. A., García-Granda, S., García, J. R., Martínez-Blanco, D. & Mohamed, S. H. Morphological and magnetic properties of the hydrothermally prepared α-Fe_2O_3 nanorods. *Mater. Chem. Phys.* **147**, 1037–1041 (2014).

Author contributions
S.G. and P.A.A. designed and performed the experiments. S.G. performed the data analysis and drafted the manuscript. P.A.A. supervised S.G. and revised the manuscript. P.A.A. wrote the scientific proposal that was the basis of this study and funded this project.

Competing interests
The authors declare no competing interests.

Additional information
Supplementary information The online version contains supplementary material available at https://doi.org/10.1038/s43246-024-00639-5.

Correspondence and requests for materials should be addressed to Parisa A. Ariya.

Peer review information *Communications Materials* thanks Jose R. Cabrero-Antonino and the other anonymous, reviewer(s) for their contribution to the peer review of this work. A peer review file is available. Primary Handling Editors: Jet-Sing Lee and John Plummer.

Reprints and permissions information is available at http://www.nature.com/reprints

Publisher's note Springer Nature remains neutral with regard to jurisdictional claims in published maps and institutional affiliations.